10-2015

A VISUALIZATION AND CHARACTERIZATION OF MICROSTRUCTURES OF COHESIVE POWDERS

Vineeth R. Patil
vrp7206@rit.edu

A VISUALIZATION AND CHARACTERIZATION OF MICROSTRUCTURES OF COHESIVE POWDERS

Vineeth R. Patil

B.Tech. Metallurgical & Materials Engineering

National Institute of Technology Karnataka Surathkal, India

A thesis submitted in partial fulfillment of the

requirements for the degree of

Master of Science in Materials Science & Engineering in the

School of Chemistry & Materials Science,

College of Science

Rochester Institute of Technology

October 2015

Signature of the Author _____

Accepted by _____

Director, M.S. Degree Program Date

SCHOOL OF CHEMISTRY AND MATERIALS SCIENCE
COLLEGE OF SCIENCE
ROCHESTER INSTITUTE OF TECHNOLOGY
ROCHESTER, NEW YORK

CERTIFICATE OF APPROVAL

M.S. DEGREE THESIS

The M.S. Degree Thesis of Vineeth R. Patil has
been examined and approved by the Thesis
Committee as satisfactory for the thesis required for
the M.S. degree in Materials Science and Engineering.

_____
Dr. Shu Chang, *Thesis Advisor*

_____
Dr. Marcos Esterman, *Thesis Co-Advisor*

_____
Dr. Scott Williams, *Committee Member*

_____
Dr. Denis Cormier, *Committee Member*

_____
Date

ABSTRACT

In this work, a framework for the determination of the particle positions in a fluorescent powder structure was created. The feasibility of imaging and quantifying sedimented particulate samples in air was demonstrated by using micron-sized poly-dispersed electrophotographic printing particles. Particle positions were determined by a Confocal Laser Scanning Microscope (CLSM) to capture a stack of cross-sectional images of fluorescent particle clusters. The resulting images were analyzed using Matlab image processing tools. The XYZ coordinates and radii for these particles (assumed spherical) were calculated in several selected sampling volumes, and the packing fractions were calculated. A three-dimensional visualization of the particle structure was then created. The CLSM particle results obtained from this study were compared with Scanning Electron Microscopy (SEM) particle imaging results. A difference in the average particle radii of the CLSM results from the SEM results was observed. The three-dimensional reconstruction of these particles showed a highly porous structure. The average packing fraction of 14.07% ± 0.84% was comparable to the literature packing fraction values for cohesive particles [1]. The cohesive nature of toner was noted from this comparison. Based on this finding, the self-similar nature of the particle clusters was investigated in the samples.

This methodology of three-dimensional particle mapping and visualization has the potential to lead to much needed materials and

structural analyses for fine particles. The frame-by-frame particle-tracking method developed in this study can be adapted into other digital imaging methods like X-ray micro-computed tomography (μCT) where the scanned object is also digitized through layer-by-layer scanning.

DEDICATION

To my parents, Raghavendra Patil & Kamala Patil, for all the unconditional love and support they have provided during my Master's degree. Although half a world away, I never felt impoverished of their care throughout the three years I have spent away from home. You have given me everything, and I am the luckiest son in the world.

To my sister, Namrata Patil, for cheering me up even in the toughest of times and for always being a support in such times.

To all my friends here and in India, without whom life would have never been the same.

ACKNOWLEDGMENTS

First, I would like to thank my advisor, Dr. Shu Chang, for all the care, guidance, support and knowledge she has provided during my thesis research. I am truly grateful to her for having accepted the task of mentoring me on this research despite all the odds faced. I feel extremely lucky to be the first student advised by her for a Master's Thesis. I would also like to thank my co-advisor, Dr. Marcos Esterman for helping me set up my experimental space initially and for being supportive during my research days. Special thanks to my committee members, Dr. Denis Cormier and Dr. Scott Williams for their professional guidance and valuable input on all parts of this thesis. Special thanks to the members of the PRISM Lab and the Next Print Lab – Dr. Alvaro Rojas, Nathan Ostrout, Heng Li, Di Bai, Mariela Rodriguez and Yuan Tian. Special thanks to Dr. Cheryl Hanzlik and Prof. Ted Kinsman for the guidance provided for the Confocal Laser Scanning Microscopy and Scanning Electron Microscopy sessions respectively.

This research is supported by the Melbert B. Cary Jr. endowment by the College of Imaging Arts and Science and by the National Science Foundation Partnerships for Innovation Building Innovation Capacity (PFI: BIC) subprogram under Grant No. 1237761. Any opinions, findings, and conclusions or recommendations expressed in this material are those of the author(s) and do not necessarily reflect the views of the National Science Foundation.

TABLE OF CONTENTS

LIST OF FIGURES

Chapter 1:

Chapter 2:

Chapter 3:

LIST OF TABLES

Chapter 3:

CHAPTER 1: INTRODUCTION

Conventional methods of manufacturing by melting and casting of materials is slowly being replaced by the use of micron-sized particles [2-6] due to the reduction in the wastage of materials and better control over the manufacturing processes [2-6]. Industrial applications using particles include processes like coating, electrostatic printing and additive manufacturing, and the materials used in these applications are governed by the Process-Structure-Property relationship. The term ‘Process’ typically refers to the set of procedures followed, including physical conditions and materials used for the manufacturing of an object in an industrial scale. Following the predefined process results in a specific ‘Structure’ (the microstructure) of the manufactured object. The microstructure plays an important role in the determination of the mechanical ‘Properties’ of the object. ‘Performance’ refers to the conditions of operating the manufactured object based on its mechanical properties. As shown in Figure 1.1, the manufacturing process used, the type of structure obtained and the properties of the structure influence the performance of these powder structures. In theory, the material and the process used for manufacturing the object determine the structural arrangement of the particles in the object.

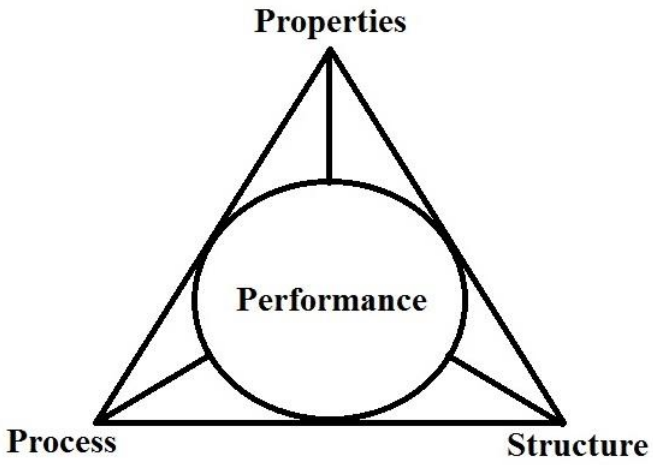

Figure 1.1 – Process-Structure-Property relationship in an industrial scale manufacturing process. The process used for manufacturing an object plays an important role in the microstructure of the object, which influences the properties of the object. The properties of the object determine the performance limitations of the object in specific scenarios.

For the determination of the material properties of an object manufactured using powder particles, it is necessary to understand the structural arrangement of the particles in tangible objects, and compare these arrangement with simulations to assess the accuracy of the simulation prediction of the structural characteristics. The structural arrangement is very important for the determination of the properties of the object that include tensile strength and creep resistance. A change in the manufacturing process could produce an unfavorable microstructure that can lead to poor mechanical properties that cause the object to fail, proving detrimental for the performance of the object. Thus, the Process-Structure-Property relationship governs the material performance of the object. Process parameters like temperature, pressure and other operating conditions can be tuned through modeling and simulations and then validated through experiments to improve the performance of the object. For example, in a

typical steelmaking process, different process parameters like the ratio of iron and carbon used, use of additives, temperature, pressure and cooling rate can be simulated and modeled to obtain various types of steels to be used in a range of applications. Thus, simulations play a major role in the development and manufacturing of objects on an industrial scale.

Particle structures are formed by inter-particle forces that are responsible for holding the particles together. When designing a manufacturing process involving microscopic granular materials, simulations can be performed for different scenarios [1, 7-17] to develop the right arrangement of the particle structure with the right properties for the manufactured structure. For example, the creation of a printed circuit using metallic nanoparticles can be simulated using complex algorithms that account for all inter-particular contact possibilities under the influence of external forces on the particles [18-22]. The simulation provides an insight on the particle arrangement in the printed circuit by determining the unknown parameters like particle positioning, particle contact scenario and contact forces between particles for the experimental verification of physical processes [20-22]. This provides a basis for the development of the right processing factors like particle deposition rate, area of deposition and the porosity of the deposited particles, which play a major role in the determination of the conductance of the printed circuit [18-22]. Furthermore, this helps to provide the insight required to design experiments for printing the circuits using nanoparticles. While simulations

help determine these experimental factors, they need not necessarily match up to the experimental results or provide the ultimate answer to the experiment performed. Thereby, post completion of the deposition, it is desirable to analyze and understand the physical structure of the deposited particles for comparison with the simulations performed.

In light of this, an experimental process is necessary to obtain the particle packing density in a dense particle structure for reconstruction and comparison with particle simulations. The methodology in this study was designed for comparison with the packing fraction results for particle simulations by performing measurements of particle positions in three-dimensional space. Measurements of the X, Y and Z positions of the particles and calculation of their radii helped to determine the packing fraction of the structures. The calculation of packing fraction helped to determine the structural arrangement of the particles in the object. By determining the microstructure of the object, a relationship to the mechanical properties of the object can be obtained, as mentioned earlier. Thus, through the packing fraction calculations, it is possible to determine the mechanical properties related to the structure of the products created by using powder particles through additive manufacturing.

1.1: Theoretical Background

This thesis utilizes the Fluorescence mode of scanning for the characterization of the powder particles, since the particles used are fluorescent. The scan type used is the XYZ scan mode, which is detailed in

the Methodology section. The CLSM uses Argon, Argon-Krypton, Helium-Neon gas lasers to generate light in the wavelength range of 352 nm to 633 nm. In the fluorescence mode used for CLSM imaging, light of a particular wavelength produced using gas lasers is focused on the particles, which triggers the excitation of valence electrons in the fluorescent materials inside the particles [23]. The electrons quickly get de-excited to the ground state, emitting photons in a range of wavelengths in the light spectrum. These emission photons are detected and converted into digital signals to generate the image. Similarly, the reflective mode [24] works on the principle of reflection of light from the samples. Reflective mode is particularly useful when the sample used in imaging is not fluorescent in nature. Since the sample particles were fluorescent in this study, the CLSM was imaged in the XYZ scan mode using fluorescence technique.

Like any optical microscopy technique, the CLSM suffers from the Point Spread Function (PSF) [20-22] along the Z-axis or XY plane of scan. An illustration of this phenomenon in the Z-axis is shown in Figure 1.2. In this phenomenon, a circular object in figure 1.2 occupying ‘a’ number of frames in the Z axis of the scan is depicted occupying ‘b’ number of Z-axis frames in the imaging, where b > a. Although the centroid of the object remains the same [25], the object appears to be elongated or stretched only in the Z-axis due to PSF as the PSF in the XY plane was corrected.

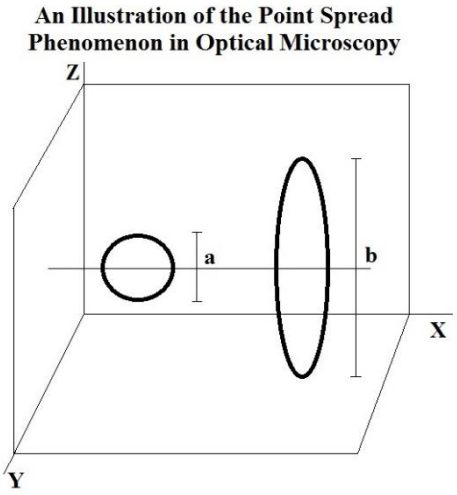

Figure 1.2: An illustration of the point spread function in optical microscopy. In this figure, a circular object occupying 'a' frames in the Z-axis is shown to occupy 'b' number of frames, where b > a.

In this study, the Z-axis PSF is neglected with an assumption that the particles are spherical with a radius equal to the XY plane radius of the particles for 3-dimensional reconstruction purposes. The particle radius in the XY plane was considered as the CLSM at RIT offered PSF correction in the XY imaging plane. However, when obtaining a 360° 3-dimensional projection of the sample imaged in the CLSM, the Leica SP-5 CLSM is provided with an imaging software suite, which has deconvolution factors built into the software for point-spread correction in the XY plane.

The images obtained in this research from the CLSM were analyzed using the *imfindcircles* function in Matlab. This function is a shape-detecting algorithm based on the 'Circular Hough Transform' algorithm. The Hough Transform algorithm is a computational algorithm which can detect lines or circles in an image [28]. This algorithm converts gray-scale images to binary images that allows the researcher to detect lines and

circles using pattern recognition [28]. The *imfindcircles* function can detect circular objects in an image and provide the size of the objects in pixel measurements. Figure 1.3 illustrates the detection of the circular particles from a particle image frame using *imfindcircles*, where all the particles present in the image were outlined with a circle.

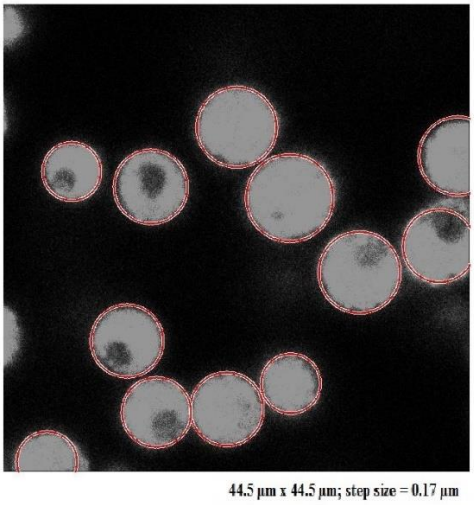

Figure 1.3 – Confocal image of particles analyzed using *imfindcircles* in Matlab. All the particles (bright circular discs) in the image are marked by a circle using the *imfindcircles* function.

The *imfindcircles* function uses three parameters [29]; ObjectPolarity, Sensitivity and EdgeThreshold. ObjectPolarity indicates the color contrast of the circular objects to the background. The default setting is 'bright', where the objects are brighter than the background in the image. Sensitivity is a parameter in the range of [0, 1], with a default value of 0.85. As the Sensitivity value is increased, the function detects more circular objects, including partial and weak circles. A very high Sensitivity value (>0.95) runs a risk of false detection of particles and must be avoided. The EdgeThreshold parameter defines the gradient threshold for determining the

edge pixels of a circular object in an image. It is set in a range of [0, 1], where a setting of 0 detects more circular objects with both weak and strong edge and a setting of 1 detects fewer circular objects with only strong edges. The output for the function is a matrix in the format [centers, radii], where the centers and radii values are in terms of pixels.

Using this theoretical knowledge, the researcher has developed a convenient method for the analysis of particle structures in this study, where the CLSM in fluorescence mode was used for imaging the clustered structures of particles and Matlab was used in processing the CLSM images. The researcher began by exploring the structural requirements of deposited powders in the electrophotographic industry and metrology using simulations, where multiple particle deposition scenarios and parameters were considered in simulating particle structures. Since the particle deposition technique used in this research was similar to Random Ballistic Deposition (RBD) simulation due to its simple nature, the researcher performed a detailed analysis of RBD, including the variations in RBD simulations. The researcher subsequently explored the prior experimental imaging techniques used for the study of particle structures as a follow up for the simulations. These techniques included Scanning Electron Microscopy (SEM), Confocal Laser Scanning Microscopy (CLSM) and X-ray Microtomography (X-ray μCT). A structural phenomenon of self-similarity observed in particle arrangement was explored in relation to the particles used in this work.

1.2: Overview of Previously Published Literature

The packing density of particle structures has been demonstrated to affect the properties of images in electrophotographic printing [1, 25]. The use of a low toner particle density in printing results in a poor quality image of low resolution, while having a high toner particle density results in a smudging and thereby bad quality of the image [30]. To print an image of optimum resolution and high quality, it is necessary to decide the right amount and mix of toner deposited on the substrate [26-28]. Simulations helped determine the exact amount of toner necessary and the charging required on the substrate to generate this high-resolution image. Thus, simulations of packed particle structures have been performed for multiple scenarios [1, 7, 8, 10-12, 14-16, 25, 29-43] for packing density calculations for the improvement of print quality in terms of the arrangement of particles. These scenarios include the method used to deposit the particles [1, 7, 8, 11, 14, 25, 29, 30, 35-39], the types of particles used [1, 7, 11, 25, 38], the sizing of the particles [34-36, 42, 43] and the influence of external forces on the particles during deposition [1, 7, 8, 30]. The simulations have been used to predict the packing density or the packing fraction of the resulting structures and their properties of mechanical strength, hardness and fatigue parameters [37].

The simulations have been broadly classified into two main categories based on the size distribution of the particles used – monodisperse [1, 12, 15, 35] and polydisperse [33, 34, 36, 42, 43]. In a

monodisperse scenario, all particles in the sample are assumed to be roughly the same size [1, 12, 15, 32-35, 42, 43]. In the polydisperse scenario, samples are considered where the particles are in a bimodal [34, 42, 43] or Gaussian distribution [33, 34, 36, 42-44]. The particle distribution used affects the packing density of the structures, obtained from the simulation [1, 10, 12, 14, 15, 29, 32-36, 42, 43]. Increasing particle size had no effect on the packing fraction of the particle structure obtained from a monodisperse particle simulation [1, 12, 14, 42]. It was observed that the packing fraction was barely influenced by the particle size in an equal-size particle distribution (monodisperse) [34, 43]. For a bimodal particle distribution, simulation using a large particle size ratio resulted in a loose packing structure, while a small particle size ratio had no significant effect on the packing fraction of the structure [34, 42, 43]. In a Gaussian particle distribution, simulation with a larger diameter range of particles in the polydisperse mixture resulted in a highly porous structure (low packing fraction) and low particle coordination number [34, 43] as opposed to a simulation with a smaller diameter range of particles in the polydisperse mixture. The simulation results have also been classified based on the adhesive properties of the powders and the use of external forces to improve the packing density of the structures obtained [12, 15, 29, 32].

Analytically, micron-size powder particle structures have been simulated with random ballistic deposition (RBD) [1, 7, 9, 11, 40] and

Discrete Element Method (DEM) [7, 9, 11, 40]. The RBD considers static conditions like particle deposition in three dimensions on a substrate [1, 7, 11, 14, 29, 30, 39, 44, 45], rolling of particles or particle restructuring [1, 7, 11, 25, 30] due to the influence of external forces on the particles for simulation purposes. Thus, RBD assumes many situations observed in a real-life deposition scenario of particles on a substrate used in this research through simple algorithms [7, 9, 11, 40]. Simple models have been developed for the better understanding of processes like colloidal sedimentation, thin-film deposition, diffusion processes and many other non-equilibrium growth and aggregation processes whose scaling properties have not been completely understood; using RBD. Discrete Element Method (DEM) is an extension of RBD in terms of particle deposition, but considers simulation dynamics that are complex in terms of calculations [34, 42, 43]. In DEM, the complexity arises as parameters like particle trajectory, particle contact angle, coordination number and contact forces between particles are tracked dynamically [34, 42, 43] as compared to RBD, which is a static simulation scenario. DEM is a calculations-heavy simulation process limited by computational power of the simulation generator [34, 42, 43].

The concept of RBD was introduced by Vold [45], while simulating the formation of a sediment by the successive deposition of equally sized particles during the analysis of cluster formations. Particles were placed at randomly selected x and y coordinates and were ‘dropped’ from infinite z

coordinate onto a substrate [45]. For a cohesion probability of 50% (where 0 = no cohesion and 99 = cohesion probability unity), 69 particles of radius 10 units were dropped in a 100 x 100 x 120 units volume cell, which yielded a packing density of 19.9%. Parameters like packing density and mean contact number (coordination number of each particle) were calculated for different cohesion probabilities and particle radii. Thus, a base paradigm was created for the exploration of RBD. In the past five decades, RBD was researched in detail and developed for various types of scenarios in particle deposition [1, 7, 11, 12, 15, 16, 25, 30, 31, 33, 34, 39-41, 44, 45, 50-53]. Some of the scenarios in the RBD simulations included:

- The consideration of adhesive particles for simulation, and the use of monodisperse and polydisperse particles to understand the effects of sizing [51-53] on the packing density in sticky [16, 25, 32, 33] and non-sticky scenarios [10, 15, 33, 35, 36, 44, 45, 54]; and
- the introduction of external forces for the rearrangement of the particles in the structures [1, 36].

These scenarios have been discussed in detail here -

RBD based on the adhesive properties and sizing of the particles used:

In the RBD simulations with cohesive powders [1, 25, 29, 31, 55], it is assumed that a cohesive particle attaches where it contacts another cohesive particle during the deposition process. This cohesiveness or stickiness creates massive voids among these particles when used for

making powder structures which result in the columnar growth of the structure [1, 36]. Jullien *et al.* and Meakin *et al.* extensively studied RBD [7, 9-11, 30, 39, 44, 45], and proposed simple models for RBD with sticky and non-sticky particles [11], RBD with restructuring [7], RBD at oblique incidence [50] and RBD with polydisperse spheres effects on packing [49]. Dependence of the width of the active deposition zone (zone where the particles are deposited on the substrate) on the mean deposit thickness was established by Jullien *et al.* [7], where the deposit thickness reduced with increasing number of contacts (coordination number) for each deposited particle [7]. The dependence of mean penetration depth (average change in the Z coordinate of the particles between the position where they first contact the deposit and the position where they come to rest at a local minimum) of particles was observed to be linear on the polydispersity of the particles [49]. Particles were deposited at vertical incidence on oblique surfaces, where the substrates were at different angles (15˚, 30˚, 45˚, 60˚, 75˚ and 87.5˚) [50] and the step size in the upper surface of the deposits increased with increasing angle of incidence [44, 50].

Meakin *et al.* also reported that particle structure simulations showed maximum particle concentration near the substrate, with waning particle concentration along the +1 direction (or the Z-axis) of the particle structures (relative to the thickness of the deposition) in sticky and non-sticky deposition situations [7, 11, 30, 39, 44, 45]. Zhou *et al.* [15] studied the packing fractions of polydisperse particle structures of different

particle size ratios. Zhou *et al.* [15] also studied the dependence of packing density and coordination number on the X and Z direction box dimensions for monodisperse particles in a non-sticky particle scenario. This study is relatable to the decision of the volume cell size to be considered for experimental analysis of monodisperse and polydisperse particle structures [15]. Ray *et al.* [22], Mal *et al.* [52] and Banerjee *et al.* [53] studied the surface properties, morphologies and scaling behavior of particles of varying cohesiveness using ballistic deposition simulations. The growth and evolution of the surface was obtained against increasing time [51-53] for varying particle cohesion probability.

In the scenario of sticky particles shown in Figure 1.4. A, the highly cohesive particles form highly porous structures such as those have been depicted in references [1, 25, 29]. On the contrary, in the other extreme scenario of non-sticky particles shown in Figure 1.4. B, where the particles have restructured under application of external forces and roll to positions of equilibriums with lower potentials as illustrated in references [1, 10, 15, 30, 32, 35, 36]. These structures show lower porosity because of the higher packing of the particles that is due to the particle rearrangement observed. Thus, sticky particle structures show low packing fraction of 14.7% [1, 36], while non-sticky particle structures show very high packing fraction of 58% [1, 15, 31]. Intermediate structures that represent those structures neither completely stick or completely not-stick show packing fractions

dependence on the contact angle parameter and under the influence of external forces on the particles.

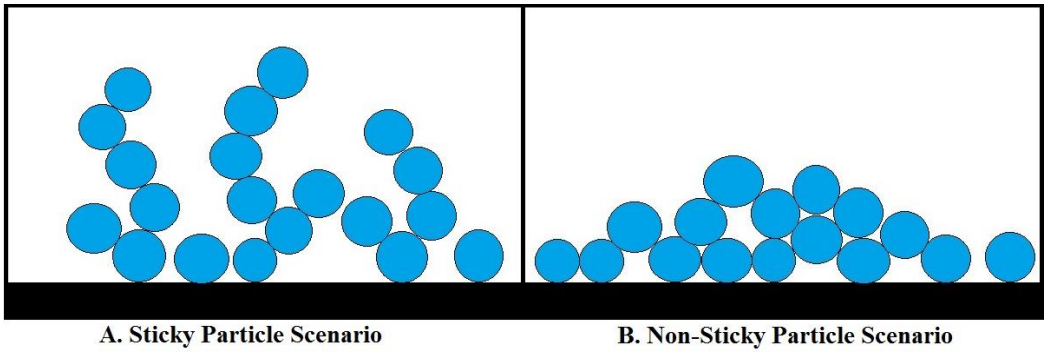

Figure 1.4 – Illustrations of A. Sticky Particle Scenario and B. Non-Sticky Particle Scenario. In the Sticky Particle Scenario, the falling particle sticks upon contact with a previously deposited particle and the critical angle of contact θ_c is 90˚. In the Non-Sticky Particle Scenario, the falling particle rolls off the contacting particle until it reaches a stable equilibrium. For this scenario, the critical angle of contact θ_c is 0˚.

Influence of external forces on the particles during RBD:

The packing fraction from restructuring of particles is based on the angles of contact among particles, where if the contacting particle is at a contact angle greater than the critical angle of contact θ_c, with the stationary particle, the contacting particle rolls over the surface of the stationary particle. See Figure 1.5.

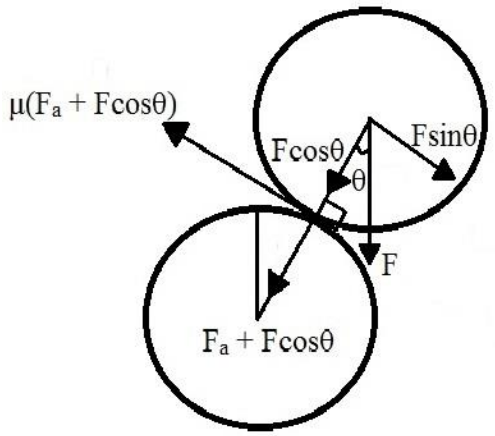

Figure 1.5 – Contact scenario between two particles with an angle of contact = θ under the influence of an external force F. When the sin component of the force exceeds the cohesive force between the two particles, the particle starts rolling on the surface of the stationary particle. (Adapted from Reference [1])

A falling particle comes in contact with a previously deposited particle at an angle θ. This angle θ is the angle of contact between the two particles. An external force F (electrostatic or magnetic) acting on the falling particle exerts a tangential force F$sin\theta$ to initiate rolling on the surface of the stationary particle to reach a stable equilibrium position. However, the particle is prevented from rolling off the stationary particle through the force of friction between the two particles μ(F_a+F$cos\theta$), which is a combination of the adhesive or cohesive force F_a and the horizontal component of the external force F$cos\theta$, with the co-efficient of friction μ. The point balance of these two forces results in a critical angle of contact θ_c between the two particles. Mizes [1] studied the angle of contact among particles in a scenario of different cohesive force and the relationship with packing fraction using spherical particles for RBD simulations. The non-sticky scenario was achieved by introducing a bias voltage to allow the

complete restructuring of charged toner particles by rolling of deposited particles to stable equilibrium positions [1]. To initiate rolling, the force F$sin\theta$ must be greater than the frictional force, where the angle of contact θ is greater than θ_c. An absence of external force F in this work causes the particles to stick together under the force μ*F_a, creating a sticky particle scenario (depicted earlier in Figure 1.4A). However, in the RBD simulations for restructuring scenario, particle rolling is facilitating for different critical angles of contact θ_c by varying the external force F [1], with the extremes at 90˚ for sticky particle scenario and 0˚ for non-sticky particle scenario.

In simulations, structures of powder particles have been inferred through their packing fraction [1, 56, 57], or the ratio of the volume occupied by particles in a cell to the total volume of the cell [56, 58, 59]. Thus, in RBD using sticky particles, cohesive particles hit-and-stick, resulting in a packing fraction of 14.7% [1, 36]. In the non-sticky scenario, particles completely restructure (or hit-and-roll) resulting in a structural packing fraction of ~ 58% [1, 15, 31]. This also establishes an inverse relationship between the packing fraction of a particle structure and the critical angle of contact θ_c [1], where the packing fraction of the structure decreases from 58% to 14.7% as the θ_c increases from 0˚ to 90˚. This research expects the particle packing fraction to be around 14.7%, since the particles in the experiment have been established as cohesive particles [1, 45].

Particle Imaging Studies:

While simulations generate particle structures for different scenarios, the experimental characterization of microscopic structures in the interior of a powder structure is difficult. Many physical characterization techniques for particle structures are unable to confirm the actual structural validity of the RBD model for hit and stick particles, where tentacle-like columnar arrangement of particles is observed [1, 36]. This is due to the fact that they either are limited to surface visualizations [3, 5, 29, 60, 61] or have been performed for packed colloidal systems where the system uses diluted solutions with suspended particles [59, 62, 63] and resembles a non-sticky particle scenario [59, 62, 63].

High Resolution Scanning Electron Microscopy (SEM) imaging has been the technique of choice to view surface microstructures formed by powders [34]. Blum *et al.* imaged the surface of an agglomerate consisting of SiO_2 micro-particles of an average diameter of 1.5 µm using a Scanning Electron Microscope [34]. The agglomerate was gravitationally deposited using laminar stream of gas in an experimental setup consisting of a cogwheel deagglomerator in a pressurized chamber [34] and a packing density of 15% was calculated for this agglomerate. Unidirectional compressional pressure was applied on the agglomerate using a micrometer stage connected to a force transducer [34]. Packing density quantification of this agglomerate was calculated as a relationship of the unidirectional compression pressure applied on the agglomerate and mass of the particles

in the agglomerate. This was performed through a power law relationship (relative change in one quantity results in a proportional relative change in the other quantity) between the compression and packing density of the agglomerate, as the particles were subject to varying unidirectional compression for densification purposes [34]. This structure was assumed to resemble an agglomerate of sticky particles obtained from simulations through packing fraction comparison [1, 34, 36]. With increasing unidirectional compressional force (up to 10^5 Pa), agglomerate structures of higher packing density up to 33% were obtained. High magnification two-dimensional (2D) micrographs from the SEM highlighted the amorphous nature of the particle structures and voids on the surface and the immediate few layers of the powders. The particles appear to be stacked on top of each other. However, it is not possible to map individual particles in the interior of the dense agglomerate using SEM imaging and the packing fraction quantification does not necessarily reflect the actual microstructures in the interior. Using SEM, it is not possible to image the particles in the lower layers or in the interior of the structure, therefore rendering the structure unquantifiable for reconstruction. Thus, it is necessary to have an imaging technique, which can be used to image and analyze particles present beneath the top-most layer of the particle structure. Confocal Laser Scanning Microscopy (CLSM) can be used in this situation.

Confocal Laser Scanning Microscopy (CLSM) has been used for three-dimensional (3D) visualization of micron-sized particles in colloidal

systems where particles are more closely packed [63-65]. Since the size of colloidal particles optimally lies near the visible spectrum of light, laser light scattering has been used for studying the dynamics of colloids [63]. CLSM can be used to resolve micron-sized individual colloidal particles due to the same reason [63]. Although lower in resolution and magnification in comparison to the electron microscopy methods as it is an optical microscopy technique, the CLSM has depth selectivity due to a controlled and highly limited depth of focus, and is capable of imaging interior structures for samples that are translucent or fluorescent in nature [24]. The CLSM has been used extensively for colloidal systems [62-65] for studying colloidal phase transitions [62-64] and reconstruction of particle structures [65].

Many studies on colloidal systems have focused on micron-sized particles [62-65]. Dinsmore *et al.* demonstration that two-dimensional tracking of particles was possible when the 1.2 μm diameter Poly-Methyl Methacrylate (PMMA) particles were suspended in the colloidal solution and in constant motion [62]. However, particles were tracked in three-dimensions upon aggregation (caused by addition of polystyrene polymers to the colloid), which slowed the particles adequately to make provisions for a full three-dimensional scan using the CLSM [62]. To avoid loss of resolution, a solvent matching the refractive index of the particles was chosen for the colloid preparation to facilitate scanning of more than 100 μm using the CLSM [62]. Similar experimental setups were used for

tracking colloidal particles using CLSM [62, 63, 65, 66]. Besseling et al. used a three-dimensional rod-fitting algorithm for tracking rod-shaped colloidal silica particles [66]. Standard microscopy glass slides and cover slips were used for sample preparation with an 85% glycerol in water solvent to correct the three-dimensional distortion of images [66]. The particles were coated with non-fluorescent outer shell to avoid overlapping of the fluorescent signals of the particles for better resolution of individual particles [66].

Prasad *et al.* [63] imaged colloidal particles consisting of monodisperse PMMA of diameter 2 μm through CLSM. Pixel by pixel reconstruction images of multiple two-dimensional plane scans of the sample was performed over a depth of 30 μm to 50 μm, scanning around 15 to 25 layers of the close packed particles [63]. Subsequent combination of these images gave a three-dimensional reconstruction of the particle structure. This three-dimensional capability is one of the inbuilt advantages of the CLSM over Electron Microscopy techniques. Although Prasad *et al.*'s reconstruction cannot be used to quantify every particle individually; the images of the variable depth scanning of the particle structure provide means for quantification of particle positions in the colloidal solution. The particle tracking in real space with the CLSM also provides an unprecedented level of information on nucleation [18, 66] and phase transitions [62, 63, 66], based on the arrangement of particles in dense colloidal particle structures [62-66].

Although CLSM imaging is limited to fluorescent particles in powders or colloids, structures consisting of fluorescent and non-fluorescent (metallic and non-metallic) powders and colloids have been visualized using X-ray Micro-computed tomography (μCT) [68-82]. This method has been used in Additive Manufacturing for non-destructive imaging and reconstruction of particle systems through systematic scanning of the sample [75, 77, 78, 81, 82]. The X-ray μCT captures stacks of images and digitally combine the images to reconstruct the object, like the CLSM [68-73, 75, 77-82], but using X-rays in place of lasers for scanning the samples. Thus, this technique has a better resolution compared to optical microscopy, reaching up to 50 nm using high-resolution zone plate lenses [81]. The object to be scanned is placed on a rotatable disc and scanned at planar rotation-based angular increments for incrementing third dimension to scan the samples [68-71, 79, 82] to obtain a multi-axial volumetric scan.

X-ray μCT has been used to study granular materials, focused primarily on obtaining the representative distributions of local void ratios of porous media, evolution of the void ratio, localized deformations of colloidal and granular materials [72, 73, 77, 78] and extraction of physically realistic pore network structure of porous media [75, 76]. Additionally, X-ray μCT has been used for density calculations of metallic objects and non-metallic powder samples [78] and quantitative three-dimensional characterization of bone implants [79]; providing a diverse range of applications for the method. Topographical metrology of the

samples is possible through this method [77], where particle distribution contours can be obtained using X-ray μCT for detailed analysis of particle distribution on the substrate.

Self-Similarity in Particle Structures:

Particle structures are known to exhibit fractal-like self-similar units during aggregation [32, 47, 55, 83-89], where parts of the structure are structurally similar to the whole structure, but much smaller in size. The particle arrangement shows similar fractal-like patterns at different magnifications of the particle structure. Kranenburg [82] observed that self-similarity for clusters of particles implied that a unique relationship existed between aggregate size and the number of primary particles that form the aggregate. Leszczynski [89] simulated particle contact scenarios for cohesive particles to obtain a model of generalized viscoelasticity operating on fractal surfaces. Gilabert *et al*. [85] observed that aggregation processes were well known to produce fractal structures, and that fractal-like networks contained denser regions and larger cavities. They also observed fractal-like regimes were observed in very-low-density samples [85]. Direct measurements of the cohesive particle aggregate structures were carried out using the method of light scattering by dilute suspensions [83, 84] and x-ray scattering [83] on silica clusters of particle size ≈ 27Å by Schaefer *et al*. [83], where fractal nature was observed in the clusters of sizes 500Å to 5000Å [83].

1.3: Research Directions

The objective of this research was to identify micron-sized particle positions in real space and produce a three-dimensional reconstruction of the particle structure. To do this work, it was necessary to have an accurate procedure to obtain the radii and coordinates of all particles in a particle structure for packing density calculations. A quantitative approach was used in this thesis for the construction of these granular particle structures and for packing fraction calculations. Unlike previous particle analysis using CLSM for studying colloidal phases and transitions [62-64, 66], this work was focused on individual particle quantification to obtain the coordinates and sizes of the particles for reconstruction purposes. As opposed to the colloidal dispersion of particles for CLSM imaging [62, 63, 65, 66], powder particles were used in this research for particle tracking using CLSM. The sample particles used in this research were stationary due to their powder nature, unlike colloidal dispersion of particles in prior research techniques using CLSM, which experienced Brownian motion [59, 62, 63, 65, 66].

In this thesis, polydisperse toner powder was used for imaging under the CLSM due to the fluorescent nature of toner components. The particles are bigger in size compared to the particles that were used in previous CLSM particle studies [62, 63, 65, 66]. The CLSM in the Fluorescence mode was used to identify the centroids of particles in a volume stack of particles. The imaging was performed with an intention to reconstruct the

particle structures three-dimensionally by obtaining the coordinates and sizes of individual particles and quantify the packing fraction of the structures. Matlab was used for the image processing to obtain the particle centroids and sizes.

The study used the resulting particle positions and radii to reproduce a three-dimensional representation of the structure formed by the particles. Comparison of the resulting packing fraction values with the simulation results calculated previously in independent research [1, 31, 55] will reveal the nature of the particles used in this work. The framework used in this thesis can be extended to determine the structures of the granular particles within a given volume. This will be used to study the self-similar nature of particle clusters in cohesive powder structures. This work can lead to the determination of particle contact parameters like coordination number (number of particles a given particle is in contact with), contact area and contact angle between two or more particles.

CHAPTER 2: METHODOLOGY

In this chapter, the topics of sample preparation, imaging of samples with the CLSM, analysis of the CLSM images obtained using Matlab, and the calculation of the packing fraction of the structures analyzed will be explained.

2.1: Sample Preparation

Emulsion Aggregation (EA) processed Electrophotographic (EP) Yellow toner from a laser printer cartridge was used to create the samples for analysis. The toner consists of numerous sub-particles including the ink pigments enclosed within the polymer shell. These pigments are fluorescent in nature and appropriate for use in the CLSM. A big challenge with using toner is that it contaminates the surfaces by adhering to the surface upon contact. Hence, a method was devised to seal the toner particles while retaining the particle structures. For this experiment, toner from different cartridges was used to create nine samples for imaging under the Confocal Microscope to maintain sample diversity.

A cover slip and a microscopy slide were used to create the samples. Cover slips were not used on top and bottom to prevent specimen loading compatibility issues with the CLSM. Using double-sided tape, an enclosure was created on a microscopy cover slip. The toner particles were dropped on a clean cover slip in the absence of an external field. The cover slip was used as a base to improve the image quality since the sample is exposed to more light with a thinner cover slip as compared to a thicker glass slide. The particles were sealed by gluing and attaching the glass slide over the

cover slip, without disturbing the toner. Thus, the powder particles were drop-deposited, sandwiched between microscopy glass slide and a cover slip and sealed as shown in Figure 2.1.

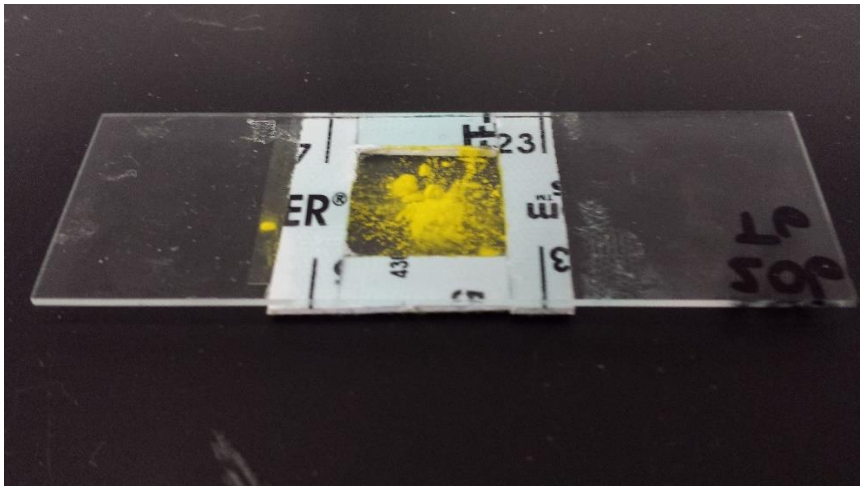

Figure 2.1 – Sample setup. Sample is prepared by encasing toner particles within a sealed setup using microscopy glass slide, cover slip and double-sided tape. The encasing prevents the smudging of toner to preserve the structures formed by the toner.

This arrangement was used for two reasons: (1) generation of thick but image-able particle structures and (2) CLSM calls for transparent substrates for the transmission of light. Transparencies were not used as substrates for sample preparation to avoid the scattering of laser beams and subsequent blurring of images, as they consist of features which do not transmit light as well as glass [91].

2.2: Imaging Methodology

The Confocal Laser Scanning Microscope (CLSM) at the College of Science, Rochester Institute of Technology, was used for imaging the particles in this study. This CLSM is a Leica SP5 Biological Confocal

microscope with a reduced out-of-focus blur function. The system used for imaging has a lateral pixel size of approximately 48 nm × 48 nm with a Z-axis sampling step of 0.17 µm. The CLSM was imaged with a 40x objective (numerical aperture = 1.1) and water as the refractive medium on the objective lens of the CLSM. The microscope has a high efficiency spectral photometry/spectrophotometer detector which uses five channels simultaneously that deliver bright, noise-free images with minimal photo damage at high speed in two different modes – Fluorescence mode and Reflective mode. The sample was imaged in the fluorescence mode with an excitation wavelength of 465 nm, generated from an Argon Laser. The photon emissions from the fluorescence were collected in the range of 476 nm to 610 nm wavelengths.

The two-dimensional planar CLSM images in the fluorescence mode consisted of bright fluorescing particles in a dark background. The dark background was observed due to the absence of the fluorescing particles and was the porous space among the particles. The brightness of the particles was adjusted using the fluorescence intensity scale in the imaging software. The scan mode was set to XYZ to obtain multiple XY images at predetermined Z increments. The XYZ scan mode digitally split the sample specimen into different layers along the Z-direction (based on a parameter called step-size). It then obtained the fluorescence image for each layer and stitched all the images together into a 3-dimensional block image in the imaging software interface for the CLSM.

Planar imaging areas consisting of multiple particle clusters were identified, within which individual sampling areas consisting of small particle clusters were magnified and stacks of XY images were collected. Since the sample was drop-deposited, the particle density was not uniform across the sample, and the clusters with low number of particles were chosen for imaging to avoid imaging issues due to the attenuation of fluorescence signals from very dense particle agglomerates. Thus, the imaging areas were predetermined by the researcher based on the visibility of all particles in the clusters. Figure 2.2 shows a large sample image area of the dimensions 237.60 µm by 216.00 µm, consisting of multiple particle clusters.

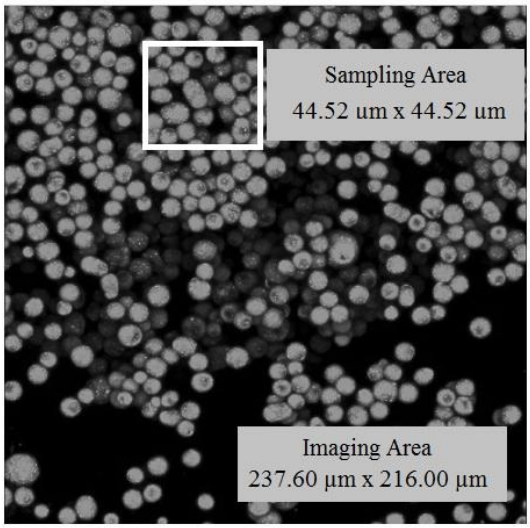

Figure 2.2 – CLSM Image of an area covered with toner particles. The imaging area is of the dimensions 237.60 µm by 216.00 µm. A large number of particles are seen as multiple clusters in the imaging area. For the particle tracking process in this study, a small sampling area of the dimensions 44.52 µm by 44.52 µm was selected as shown by the boxed area.

A closer observation of Figure 2.2 shows the particles in the foreground appear to be clearer and brighter than the other particles in the background. This was because the clearly observed particles are closer to the photomultiplier detector of the CLSM and have no obstacles in the imaging path as they were at the base of the sample. Smaller sampling areas were selected as regions of interest for analysis from the bigger clusters observed (like the one shown in Figure 2.2). This selection was entirely based off the visibility of the particles in the imaged clusters. A sampling area of 44.52μm by 44.52μm was selected to image the particle cluster in this imaging area, roughly to simulate a 600 dots per inch printing addressability [91]. In the XYZ scan mode used in the experiment, the sample was divided into multiple steps and scanned step-by-step from the base to the top. An example of the Z-step scanning for a particle structure is shown in Figure 2.3. The step thickness was set to 0.17 μm along the vertical axis or the Z-axis of the sample and the sample was scanned continuously from the base to top at a stepping rate of 0.17 μm using the sensitive stepping motor. This was based on the observation that the particle density was the highest at the base of the sample (cover slip) and decreased with increasing Z height. CLSM XY planar images numbering from 100 to 300 were obtained for each stack, stored in J-peg format and converted to grayscale for analysis using Matlab.

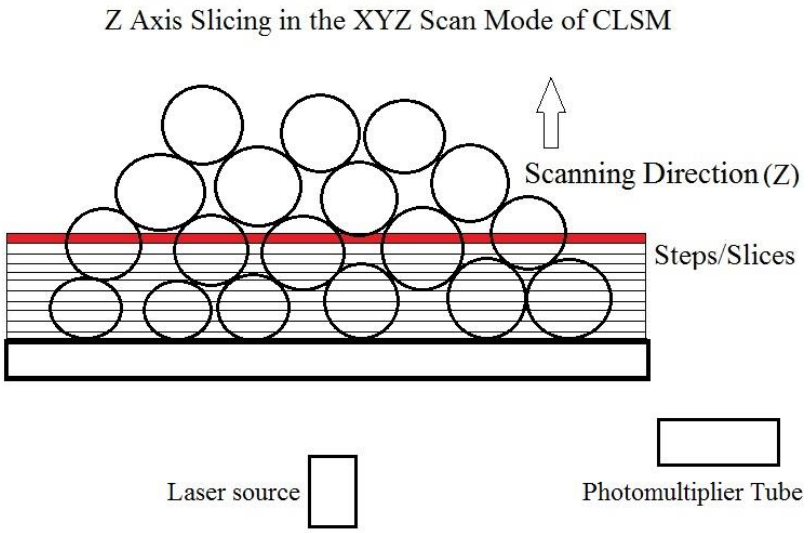

Figure 2.3 – Illustration of the digital sample slicing along the Z-axis in the XYZ scan mode of the CLSM. The structure was digitally sliced into multiple steps, where each step thickness is equal to the step size set in the CLSM. The sample was imaged in the XY plane at every Z step. The scanning direction was from bottom to top, where the layer marked in red shows the current step being scanned.

Multiple images obtained at this Z step increment were stacked together to cover the entire sample thickness. Z-depth range was based on the number of layers observed during the imaging of the particle clusters. The number of layers was limited to four to six layers, as the use of powder particles for sample preparation would lead to distortion of images due to diffraction of fluorescence emissions. This was unlike the previous literature on CLSM imaging [62, 63, 65, 66], where colloidal particles were dispersed in a solvent of the same refractive index as the particles to enable scanning of multiple layers of particles. Nine sampling volumes (from specimens created using toner from different cartridges) were selected on this basis and imaged to provide more data for a better analysis.

For qualitative analysis of the particle structures, the sample images scanned were converted into a three-dimensional frame-by-frame projection using the software suite provided for the CLSM. This three-dimensional projection provided an overview of the structural arrangement of the particles that facilitated the observation of particle layering within the structure. This process was repeated for all our samples for qualitative analysis purposes as this helped determine the number of layers present in each particle cluster that was imaged.

2.3: Image Analysis

The particles from the smaller sampling area of 44.52 µm * 44.52 µm in Figure 2.3 were considered for the image analysis. The sampling area was magnified to show the particles at a particular Z-axis value inside the structure. See Figure 2.4 for this representation. The images show the particles clearly as bright, roughly circular objects in a contrasting dark background. A random particle in the area was selected to obtain the X, Y & Z coordinates and the radius, as illustrated in Figure 2.4.

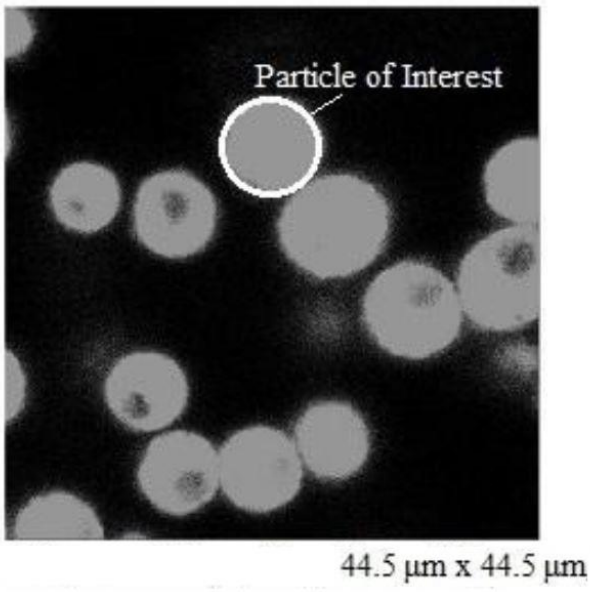

Figure 2.4 – CLSM Image from one cross-sectional plane of the sampling area where a particle is selected as the Particle of Interest.

The Z coordinate was calculated by the frame counting method, which was obtained by plotting the radius of the particle of interest increasing Z-axis in a bottom to top direction. In this analysis, the particle 'starts' from the frame when it appears in the XY cross-sectional image and 'ends' at the frame where it disappears in the image at a particular depth. This method estimated the Z centroid of the particle for the frame where the radius of the particle of interest was the highest. Figure 2.5 illustrates this using the cross-sectional images for a particle at three different depths to illustrate this radius change at different Z values.

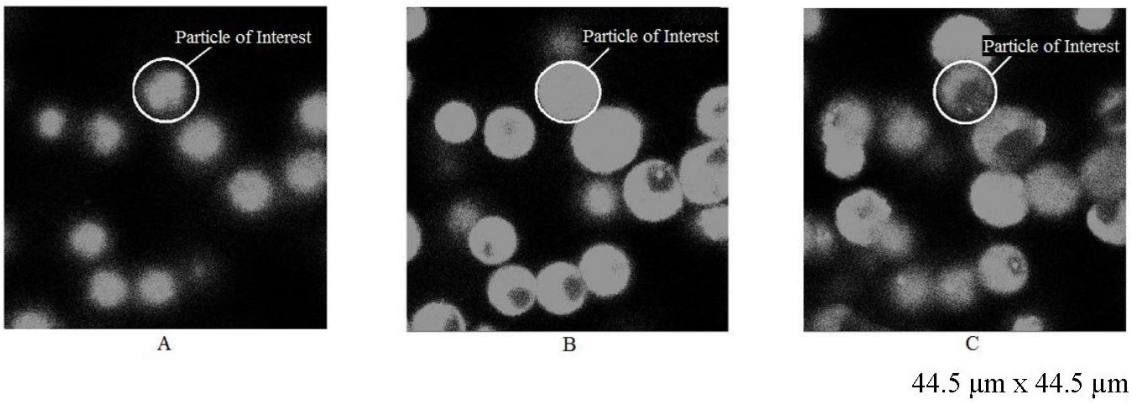

Figure 2.5 - Methodology to obtain the Z position for the Particle of Interest. The dimensions of this volume cell are 44.5 µm by 44.5 µm by 32.2 µm with a Z-step sampling size at 0.17 µm. The Z position for the particle of interest in A is 4 µm, in B is 9.2 µm and in C is 13 µm. As shown here, the maximum-radius frame is closer to image B than those of A and C.

For all particles, as the size of a particle increased in the image stack, the number of fluorescing pixels increased, causing the particle to appear bigger and brighter. Beyond the center plane of the particle, the particle 'disappeared' or blurred out of the image as the number of fluorescing pixels decreased. A result of the frame counting method to obtain the Z coordinate of one of the particles is shown in Figure 2.6. The particle in focus was imaged at incrementing steps of 0.17 µm using the CLSM. Using the *imfindcircles* function, the radius of this particle was calculated on every frame. The frame radii were plotted as shown in Figure 2.6. The results indicated a steady increase in the particle XY plane radius of the particle with increasing Z-axis measure, until the maximum point was reached; the particle XY plane radius then decreased at a steady rate. For the particle analyzed in Figure 2.6, the XY plane radius was 4.40 µm, while the Z radius was 10.40 µm (Z diameter = 20.80 µm).

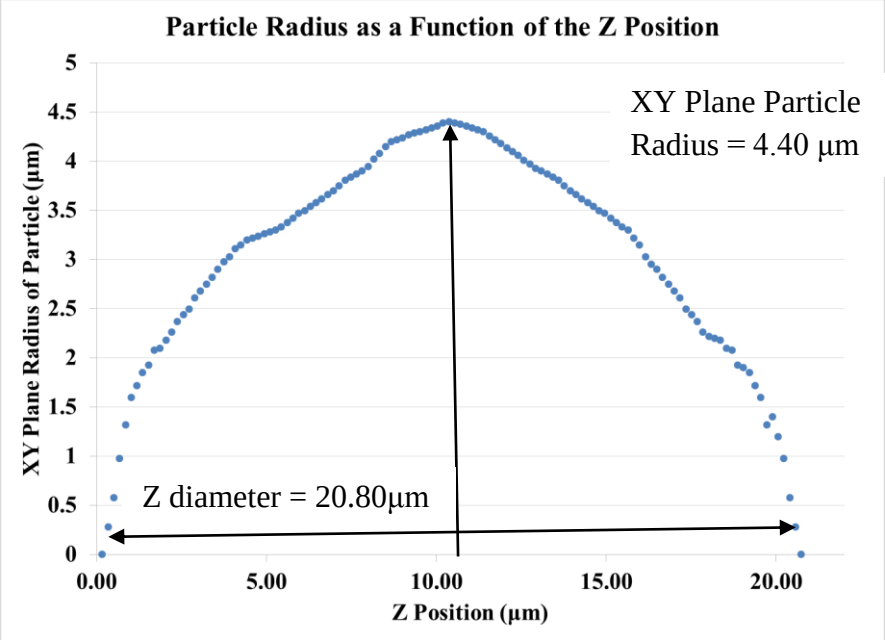

Figure 2.6 – Particle radius as a function of increasing Z position. A steady increase in the radius along with increasing Z-axis was observed until the Z centroid of the particle, after which a steady decrease in radius was seen until the particle disappears. In this figure, the point of maxima was at 10.40 µm, where the XY radius of the particle was 4.40 µm. Although the particle suffers from PSF along Z-axis, the centroid remains the same [25-27], as PSF is an optical image elongation around a fixed point.

The point of maxima was considered as the center Z coordinate of the particle, with the true radius of the particle being the difference between the point of maxima and the point of minima along the radius axis of Figure 2.6. The corresponding frame was used for the calculation of the X & Y coordinates of the particle in the XY plane. While the XY radius of the particle is 4.40 µm, the particle is elongated on the Z-axis by over two times the XY radius, indicating that particle is prolate-spheroidal in shape. This elongation is due to Point Spread Function (PSF) along the Z-axis. The maximum-radius z-position frame identified in Figure 2.6 was used as the image frame for the analysis of X and Y values for the "particle of interest".

To identify the X and Y coordinates and the radius for the particle of interest, the Matlab imaging function imfindcircles was used.

Since the particles were observed as bright objects in a dark background, the ObjectPolarity parameter was set as 'bright' in the *imfindcircles* function parameters. To improve the detection of the edges of the particles with the best possible accuracy, the Sensitivity and EdgeThreshold parameters were set at 0.95 and 0.1 respectively. Using a command line Edgecircles = viscircles('center','radii'), the circles were enabled to be marked on the image around the particle edges. The *imfindcircles* function was used to locate the X and Y coordinates for the center of the particle and radius, as shown in the Figure 2.7 using the Z-centroid CLSM image frame.

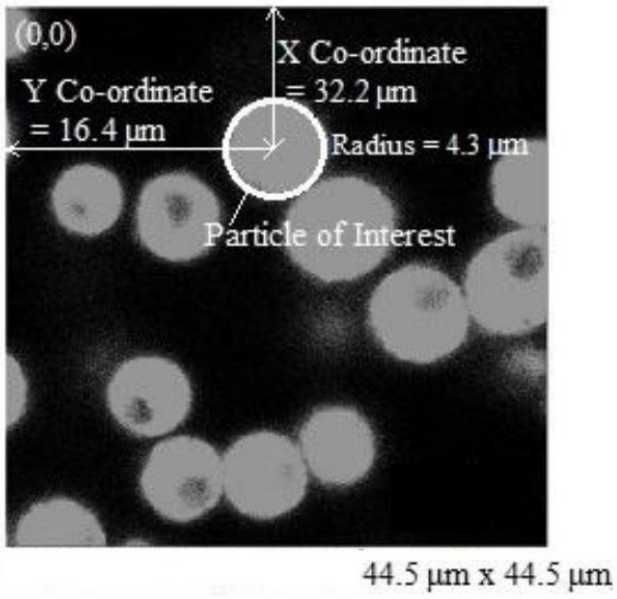

Figure 2.7 – CLSM image denoting the origin in the image, X and Y coordinates and the radius of the particle of interest. For this particle of interest, the X and Y coordinates are at 32.2 µm and 16.4 µm with zero located at the top-left corner respectively and the radius is 4.3 µm.

The command line for the *imfindcircles* function was -

[centers, radii] = imfindcircles(imagename,[RMin RMax],

'ObjectPolarity','bright', 'Sensitivity',0.95, 'EdgeThreshold',0.10)

RMin and RMax define the size range of the particles using the expected minimum and maximum in pixel values. In the image analysis using *imfindcircles* shown in Figure 2.7, the origin was always set at the top left corner of the image. The X-axis increased from the left to right of the image, while the Y-axis increased from the top to bottom of the image. This analysis method was performed until all the particles in the 3D image stack were analyzed. The procedure was repeated for all samples analyzed.

The framework for obtaining the particle coordinates and radii was summarized, as in Figure 2.8. Step one in the particle analysis began by selecting a particle for analysis from the stack of particles scanned by the CLSM. The Z coordinate of the particle was obtained using the frame count method, with the center frame of the particle calculated as the Z coordinate value. The X & Y coordinates and the radii of the particles were obtained by analyzing the Z center frame using *imfindcircles* function in Matlab. Automation of the steps mentioned above increased the analysis rate of multiple particles in the samples. The coordinates and radii of the particles obtained by this analysis were plotted in a 3-dimensional space, using graph tools in Matlab.

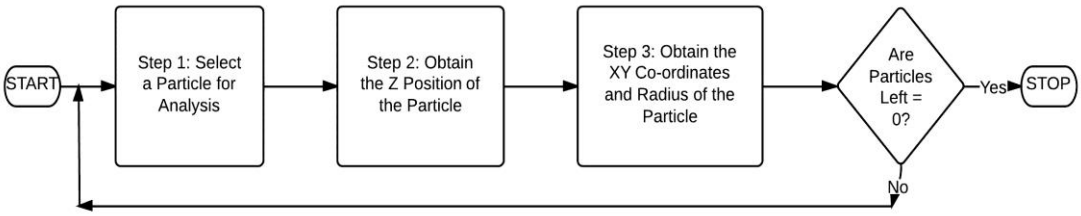

Figure 2.8 - A three-stepped process to obtain the particle coordinates and radii.

2.4: Packing Fraction Calculations

For measuring cell volume, partial particles were considered for packing fraction calculation based on the percentage of the particles present in the volume cell. See Figure 2.9. The particles shaded gray were considered for the calculation of the total volume of the particles, while the parts of particles shaded in black were excluded from the analysis. For the particles that were partially present inside the volume cell, the partial volume of particles was calculated as an approximation of the percentage of particle present in the volume cell from the visualization of the particle. For counting purposes, the partial particles were counted as whole numbers, where if a particle was present 50% or more by volume inside the volume cell, it was counted as one particle towards the total number of particles present in the volume cell. For the calculation of the packing fraction, the volume unit cell for every sample was considered as a cube or a cuboid, as shown in Figure 2.9.

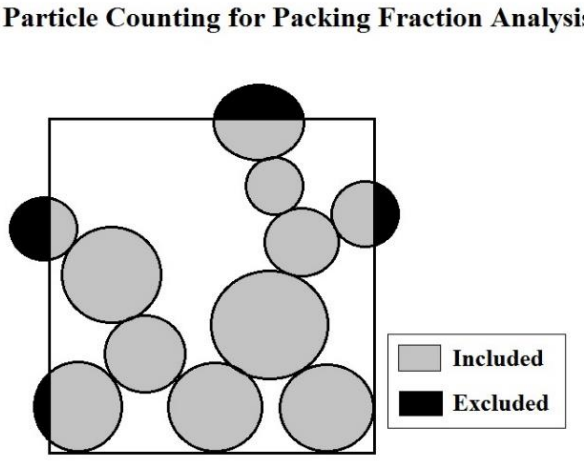

Figure 2.9: Particle counting for calculation of the packing fraction. For the particles shown in the box, the particles shaded gray are included in the particle volume calculation, which involves partial particles as well. The partial particles shaded in black are excluded from the analysis.

The packing fraction of the analyzed particle volume cell was calculated as the ratio of the total volume of all particles within the sample cell (Vp) divided by the volume of the particle cell (Vc) [91, 92]. The total volume occupied by the particles within the volumetric unit can be summed up from each particle within the sampling cell and each partial particle on the cell surfaces, edges and corners. The total volume of the particles within the cell, denoted Vp, can be calculated from:

$$\mathrm{Vp} = \sum_i Vi\ (interior) + \sum_j Vj\ (surfaces) + \sum_k Vk\ (edges) + \sum_l Vl\ (corners) - \sum_m Vm\ (particles\ double\ counted\ overlapping\ volumes) \quad \ldots\ldots\ (2)$$

Where i = number of particles in the interior, j = number of partial particles residing on the 6 surfaces and excluding those on the edges and at the corners, k = number of partial particles on the 12 edges and excluding those

at the corners, l = number of partial particles at the 8 corners and m = number of particles that overlap the neighboring particles, all within the cubic cell of dimensions - w (width), h (height), and d (depth). The packing fraction of the particle structure, denoted as ϕ, is then:

$$\phi = \frac{Vp}{Vc} = \frac{Vp}{w*h*d} \quad \text{……………………………………} \quad (3)$$

CHAPTER 3: RESULTS

The results chapter consists of the comparison of the CLSM particle size distribution results with the Scanning Electron Microscope (SEM) results using Statistical Analysis methods, Matlab and Rhino 3D reconstruction of a particle volume cell using the XYZ coordinates and size of the particles and packing fraction calculation of all the samples analyzed under the CLSM. Statistical tests were conducted to verify the results obtained from the experimental steps explained in Chapter 2. The particle analysis results have been elaborated upon using these statistical tests in this chapter to conclude to the goals of this research.

3.1: Particle Distribution Analysis

For the statistical analysis performed in this section, two hypotheses conditions were formulated based on p-values. A Null Hypothesis (H_0: data is normal) was defined to check for the normality of data; it was checked using a p-value of 0.05. It is vital to check for normality of data as a t-test or ANOVA assumes the sample(s) to be normal. Similarly, an alternative hypothesis (H_a: data is non-normal) was defined to imply the non-normality of the data. For a statistical test that resulted in a p-value greater than 0.05, the researcher failed to reject the Null Hypothesis – concluding that the data was normal. The Quantum XL add-on for MS Excel was employed for creation of the particle distribution histogram. Minitab was used for the Normality test. A particle distribution analysis chart for the radii of all particles obtained using CLSM, is presented in Figure 3.1 to show the polydispersity of the particles used in this work. The results produced a mean particle radius of 3.40 μm and standard deviation of 0.66 μm for a

sample size of 126 particles. Anderson-Darling test was performed to check the probability distribution of the data, in this case a normal distribution, shown in Figure 3.2. Since the p-value = 0.86 > 0.05, the researcher failed to reject the Null Hypothesis. The range of the particle radius was from 1.7 µm to 5.1 µm, which reflects the polydispersity of toner.

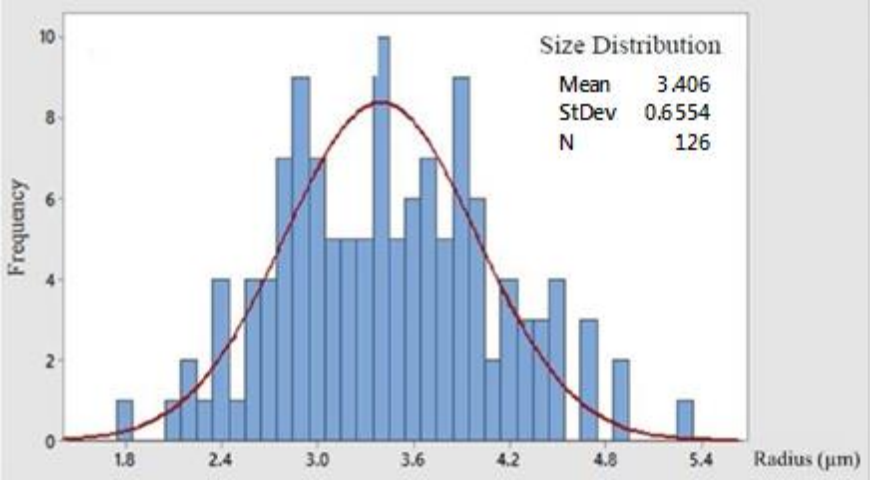

Figure 3.1 – CLSM radius distribution of toner particles. The mean particle radius is 3.40 µm and the standard deviation (σ) is 0.66 µm for 126 particles, which reflected polydispersity. The normality check of the data in Figure 3.2 showed a normal distribution.

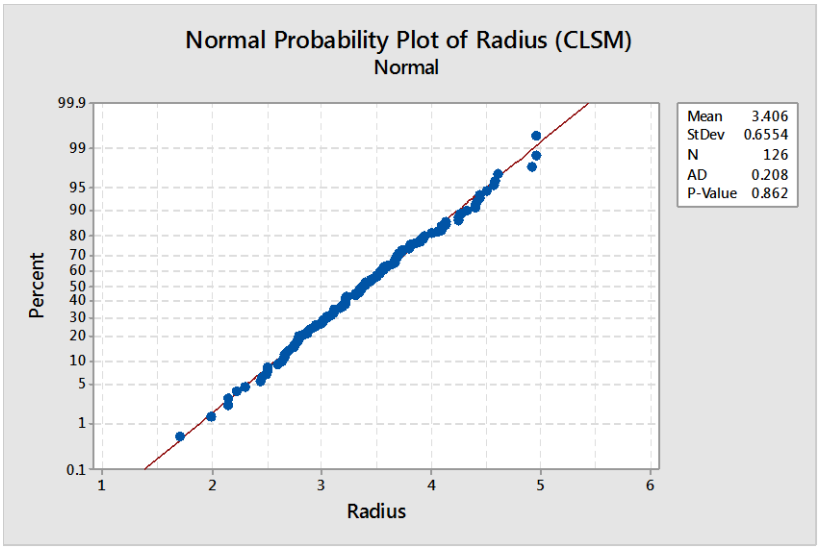

Figure 3.2 – Normality test plot for the CLSM radius distribution using Anderson-Darling method. The researcher failed to reject the Null Hypothesis that the data was of a normal distribution based on a p-value = 0.86 > 0.05.

A similar experiment for toner analysis was done using SEM by *Bai et al.* [92], to check the accuracy of the CLSM imaging. Toner from the same cartridge source (used in this experiment) was used for creation of samples for imaging under the SEM. The SEM imaging was performed with a JEOL-JSM-6100 system. Spheroidal toner particles were considered for the particle distribution analysis, while the ellipsoidal particles and agglomerates were excluded [92]. The SEM particle distribution results are shown in Figure 3.3. The SEM toner particle analysis showed a mean particle radius of 3.59 µm, with a standard deviation of 0.66 µm for 1234 particles [92]. The SEM analysis showed the particles of the size range 1.8 µm to 5.4 µm. In addition, a normality check of the SEM data using the Anderson-Darling test gave a p-value = 0.27 > 0.05, shown in Figure 3.4. Once again, the researcher failed to reject the Null Hypothesis.

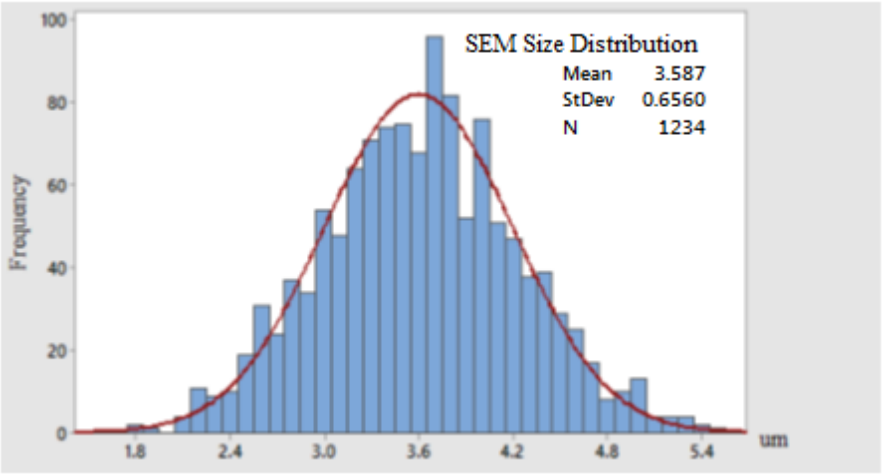

Figure 3.3 – SEM radius distribution of toner particles [92]. The mean particle radius is 3.6 µm and the σ is 0.7 µm for 1234 particles, and shows a normal distribution, which reflects polydispersity.

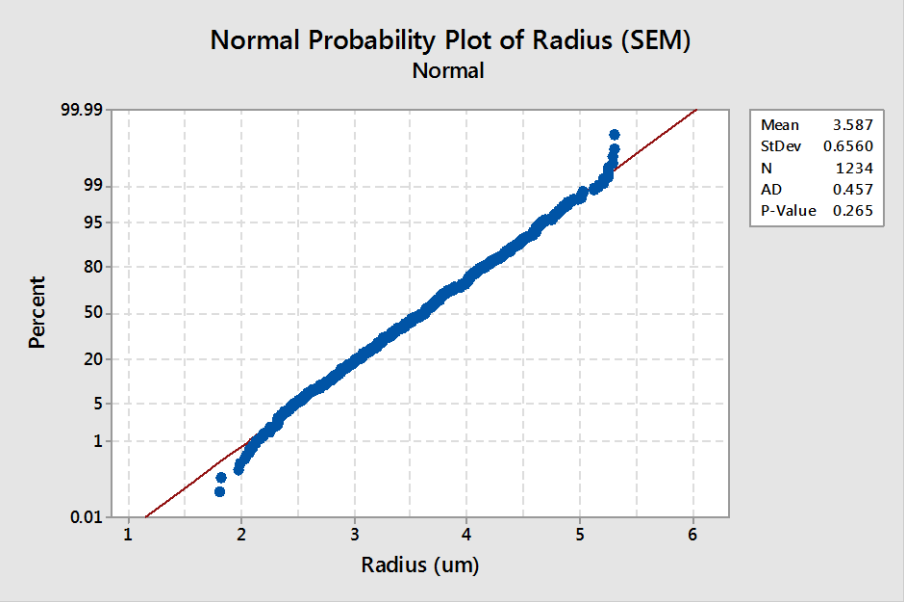

Figure 3.4 – Normality test plot for the SEM radius distribution using Anderson-Darling method. The researcher failed to reject the Null Hypothesis that the data was of a normal distribution based on a p-value = 0.26 > 0.05.

Since the assumption of Normality of data for both CLSM and SEM samples was accepted based on the failure to reject the null hypotheses, a two-sample t-test was used to compare the means of CLSM and SEM samples. See Figure 3.5 for the 95% Confidence Interval (CI) Mean comparison results. A Null Hypothesis (H_0: $\mu_{CLSM} = \mu_{SEM}$) was defined to check if the means are the same; it was checked using a p-value of 0.05. Similarly, an alternative hypothesis (H_a: $\mu_{CLSM} \neq \mu_{SEM}$) was defined to imply that the means are different. A p-value = 0.003 (< 0.05) shows that the CLSM data was statistically different compared to the SEM data. A significant p-value led to the rejection of the Null Hypothesis.

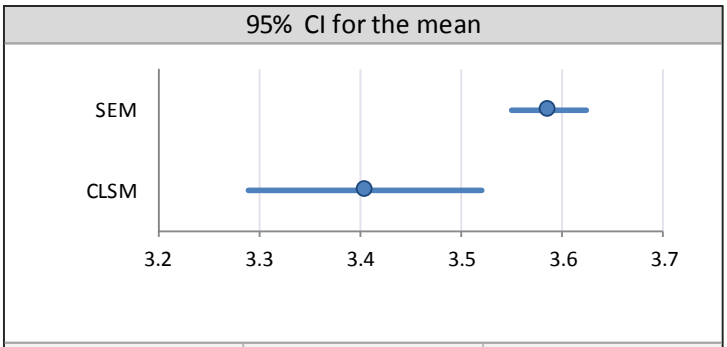

	CLSM	SEM
Lower Bound	3.29	3.5508
Upper Bound	3.5211	3.6241

Figure 3.5 – 95% Confidence Interval Mean comparison for the two-sample t-test comparing the CLSM and SEM radii. The means do not overlap, indicating the difference between the CLSM and SEM samples. The researcher rejected the Null Hypothesis and the samples were not matched, based on a p-value = 0.003 < 0.05.

The t-test for the CLSM data and the SEM data showed a deviation in the means of the CLSM and SEM results. This result was due to the sample size difference between the CLSM data and SEM data. A larger sample size (SEM in this case) has a tighter Confidence Interval (CI) compared to a smaller sample size (CLSM in this case), due to which they fail to overlap – hence the difference. The smaller radii values from CLSM imaging compared to those from the SEM imaging could be from diminishing fluorescence emissions along the particle edges.

Data analysis of the particles of every sample shows the polydisperse nature of the samples used for the analysis, with a mean radius value of 3.40 µm. See the generated particle distribution box plot of the individual CLSM samples, shown in Figure 3.6. This graph was generated using JMP Statistical Data Analysis software. The observed samples had a mean particle radius around the mean particle size of 3.40 µm, while the particles

present in every sample are in a range of radii, showing polydispersity. The particles in the imaging volume were selected as described in Section 2.4 of Chapter 2. Samples 5 & 6 show only 8 particles each, while some samples show more than 11 particles. The samples 5 & 6 were imaged at a higher digital magnification compared to the other samples, thus the number the particles was lower. Sample 1 was imaged at a lower digital magnification, thus accounting for a larger number of particles compared to the other samples.

Based on the normal distribution of the CLSM samples, parametric tests were used to check if the samples were the same. A Null Hypothesis (H_0: $\mu_{Sample1} = \mu_{Sample2} = \ldots = \mu_{Sample9}$) was defined to check if the means were the same; it was checked using a p-value of 0.05. Similarly, an alternative hypothesis (H_a: $\mu_{Sample1} \neq \mu_{Sample2} = \ldots = \mu_{Sample9}$) was defined to imply that at least one sample mean was different from others. The All-Pairs Tukey-Kramer test for sample pair-wise comparison for the purpose of sanity check, which is similar to the t-distribution in a t-test, was performed since the sample sizes (number of particles per sample) were unequal. The graphical result was published along with the sample box plots in Figure 3.6.

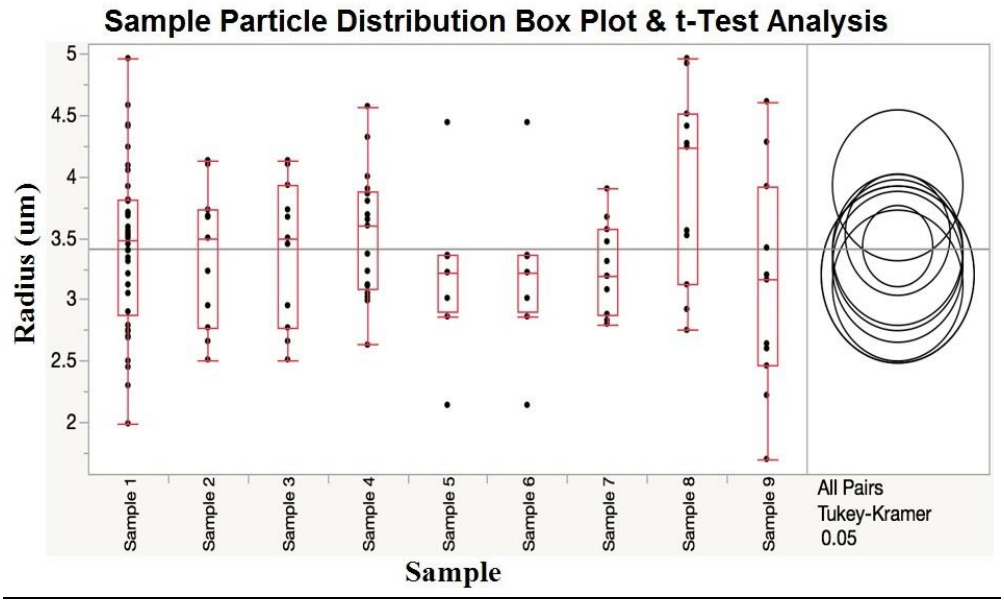

Figure 3.6: Sample-wise box plot of particle size distribution. ANOVA test (See Figure 3.7) shows that the samples are similar to each other. An All-Pairs Tukey-Kramer test shows no significant difference amongst the samples, further indicating the similarity amongst the samples irrespective of the sample size.

Each ring from the graphical result represents the confidence interval for a sample, and overlapping circles indicate no significant difference among the samples. An ANOVA of the samples shown in Figure 3.7 gave a p-value = 0.15 > 0.05, which showed that all samples are statistically similar to each other in terms of the particle size. Since the p-value was greater than 0.05, the researcher failed to reject the Null Hypothesis. Thus, the samples were statistically determined to be conducive for structural analysis comparison.

Oneway Anova

Summary of Fit

Rsquare	0.095501
Adj Rsquare	0.033655
Root Mean Square Error	0.644054
Mean of Response	3.405556
Observations (or Sum Wgts)	126

Analysis of Variance

Source	DF	Sum of Squares	Mean Square	F Ratio	Prob > F
Sample	8	5.124232	0.640529	1.5442	0.1494
Error	117	48.532279	0.414806		
C. Total	125	53.656511			

Means for Oneway Anova

Level	Number	Mean	Std Error	Lower 95%	Upper 95%
Sample 1	38	3.43105	0.10448	3.2241	3.6380
Sample 2	11	3.35727	0.19419	2.9727	3.7419
Sample 3	11	3.40000	0.19419	3.0154	3.7846
Sample 4	17	3.52412	0.15621	3.2148	3.8335
Sample 5	8	3.20000	0.22771	2.7490	3.6510
Sample 6	8	3.20000	0.22771	2.7490	3.6510
Sample 7	11	3.26273	0.19419	2.8781	3.6473
Sample 8	11	3.92545	0.19419	3.5409	4.3100
Sample 9	11	3.11000	0.19419	2.7254	3.4946

Std Error uses a pooled estimate of error variance

Figure 3.7 – One-way ANOVA (Analysis of Variance) test results for the CLSM samples. The researcher failed to reject the Null Hypothesis that all samples are similar irrespective of the number of particles per sample, based on a p-value of 0.26 (> 0.05).

3.2: 3-Dimensional Reconstruction of Particle Structures

The XYZ position & radii calculations for Sample 1 (among the nine CLSM samples) were performed for the remaining particles in the sample and the results are presented in Table 3.1.

Particle No	X (µm)	Y (µm)	Z (µm)	R (µm)	Particle No	X (µm)	Y (µm)	Z (µm)	R (µm)
1	14.24	38.80	3.55	3.51	20	39.98	0.95	12.45	4.14
2	33.83	25.59	3.89	3.83	21	32.49	42.96	13.28	2.80
3	4.22	43.23	4.05	3.25	22	3.26	32.42	14.46	2.84
4	43.41	14.99	4.05	3.52	23	1.05	15.60	14.63	3.14
5	21.51	38.91	4.22	3.51	24	10.01	35.06	15.47	1.95
6	12.09	31.66	4.39	3.25	25	18.49	20.54	15.68	2.95
7	40.56	23.60	4.39	4.38	26	5.31	38.26	16.31	2.40
8	22.30	11.40	4.72	3.97	27	29.01	5.32	17.65	3.24
9	27.54	18.36	4.89	4.71	28	33.54	39.71	20.33	3.59
10	6.71	15.96	5.06	3.32	29	18.25	32.64	21.68	3.35
11	14.15	17.21	5.23	4.04	30	31.59	32.21	22.18	3.16
12	12.30	15.89	5.73	3.32	31	26.99	0.51	22.35	2.29
13	27.64	36.14	5.90	3.48	32	8.13	9.86	24.70	4.52
14	32.72	17.38	6.40	3.14	33	13.52	20.38	24.86	3.84
15	26.71	26.40	9.59	3.48	34	34.19	4.76	25.20	1.45
16	24.55	27.33	9.76	4.19	35	16.94	26.98	26.88	2.54
17	7.69	28.78	9.93	3.39	36	18.82	14.47	27.45	2.54
18	22.10	4.74	10.93	3.53	37	38.73	42.59	28.56	3.10
19	5.62	20.42	11.10	3.07	38	42.45	8.89	28.56	2.18

Table 3.1 – XYZ coordinates and Radii (R) (in µm) of the particles from Sample 1. The dimensions of the volume cell are 44.5 µm x 44.5 µm x 27.2 µm. A total of 38 particles were present in the sample, with a mean particle radius of 3.62 µm.

From Table 3.1, the measured XYZ coordinates and radii values for each unit cell were used to reconstruct into a 3-D image in Matlab and Rhino 3D. Figure 3.8 depicts the reconstruction of the sample presented in Table 3.1 and the packing fraction results associated with it. Point Spread Function (PSF) observed in Figure 2.6 was ignored by treating the particles as spherical with Z-axis radius equal to the XY plane radius.

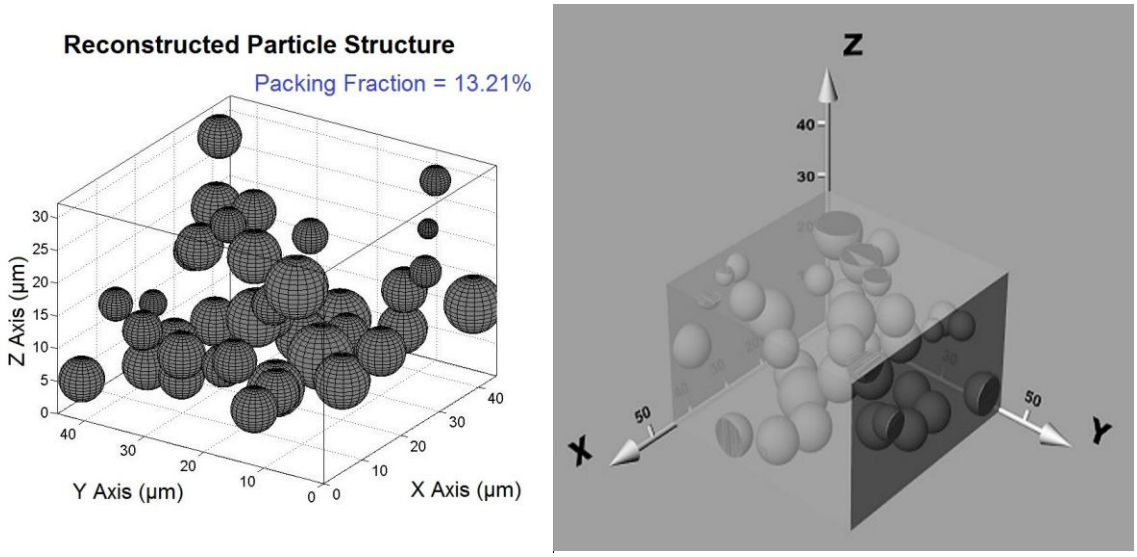

Figure 3.8 – Matlab (left) and Rhino3D (right) reconstruction of a particle volume cell from Table 3.1. The volume cell is of the dimensions 44.5 µm x 44.5 µm x 27.2 µm. The "suspended" particles are in contact with particles in the neighboring volume cells, which are supporting them. The Rhino 3D reconstruction depicts the partial particles present in the volume cell. The packing fraction of this volume cell is 13.21%. Credits to Di Bai for help with the Rhino 3D reconstruction.

The particle reconstructions in Figure 3.8 illustrate the openness of the particle structure. This openness of the sample is attributed to the cohesive nature of the toner particles used for the experiment. Note that there appears to be some particles "suspended" in space. However, these particles are in contact with and supported by particles in the neighboring volume units. The partial particles were depicted as sliced off partial spheres in the Rhino 3D reconstruction. Due to the dimensional restriction of the sample analyzed during imaging, the contacting particles of the neighboring units were not depicted in the reconstruction. Similar calculations were performed for the remaining eight samples imaged under the CLSM.

The reconstruction in Figure 3.8 yielded a packing fraction value of 13.21%, indicating 86.79% of the structure is unoccupied, leading to a

conclusion of a highly porous structure. A layer-by-layer analysis of the particle structure of Figure 3.8 is shown in Figure 3.9. For this analysis, the XYZ mode images were analyzed. The particles were differentiated into layers based on the disappearance of the bulk of the particles with increasing Z position. Five layers of particles were found in the structure based on this analysis using increasing Z-axis. The base of the particle structure consisted of 14 particles, and subsequent layers consisted of 9, 6, 5 and 4 particles respectively. The highest particle concentration was at the base layer and then decreased with increasing Z height, as shown in literature for a ballistic deposition process [7, 11, 30, 39, 40, 44, 45].

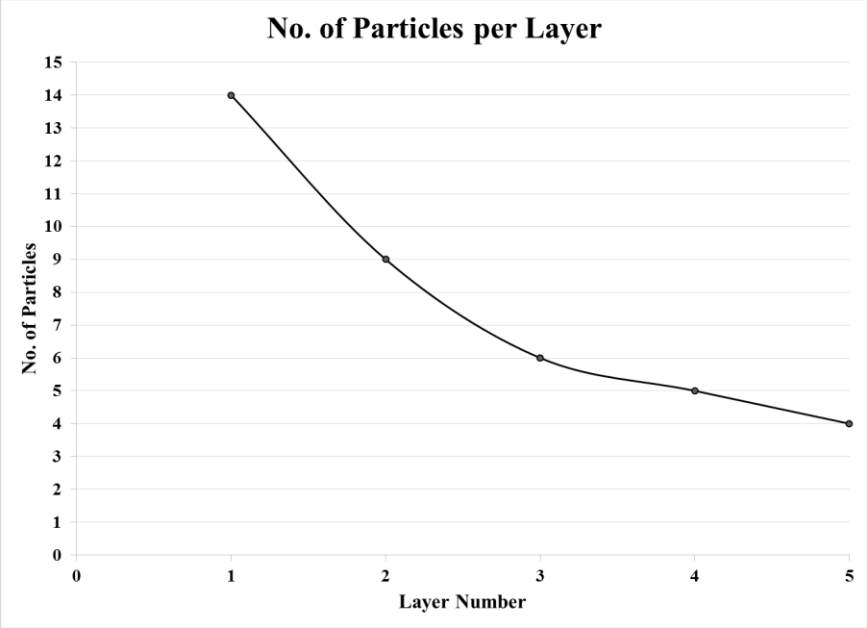

Figure 3.9 – Graphical analysis of the number of particles per layer against increasing Z-axis. We observed 5 layers of particles in the structure, with 14 particles in the base. The subsequent layers had 9, 6, 5 and 4 particles respectively.

By using this method of particle analysis, the XYZ coordinates and radii in XY planes were obtained for the nine CLSM imaging samples with

a total of 126 particles. The samples were analyzed using the automated procedure and verified individually by manual verification of the coordinates of every particle. The Packing Fraction calculations from the nine samples shown in Table 3.2 produced an average packing fraction of 14.07 % with a 0.84 % standard deviation as reported in the researcher's previous publications [91, 93].

Sample No.	No. of Particles	Mean Particle Radius (µm)	Unit Cell Volume (µm3)	Packing Fraction (%)
1	38	3.43	53862.8	13.21
2	11	3.36	18269.4	13.39
3	11	3.40	14943.5	14.11
4	17	3.52	17430.6	13.42
5	8	3.20	5602.0	14.32
6	8	3.20	6065.1	14.12
7	11	3.26	11437.4	15.23
8	11	3.92	13267.4	15.52
9	11	3.11	13672.6	13.35
	Sum = 126		Mean PF	14.07%
			Std. Dev.	0.84%

Table 3.2 – Packing fraction values of all samples analyzed. We have obtained an average packing fraction of 14.07% with a standard deviation of 0.84%.

While the number of particles in each sample cluster is varying, the packing fraction values for the nine samples are very close to each other. Since these samples were parts of bigger clusters that were imaged, it could imply the self-similar nature of the cluster [82, 83, 86, 90]. A correlation graph between packing fraction and particle mean radius was plotted in JMP Statistical Data Analysis software. A correlation between the particle mean radius of each sample to the sample packing fraction from Table 3.2 showed the packing fraction is weakly correlated to the particle size. This

correlation is shown in Figure 3.10, where the X-axis is the Sample Mean Particle Radius (µm) and the Y-axis is the Particle Packing Fraction (%). While the X-Y plot shows the particle radius variation of the packing fraction per sample, the circle is the confidence interval density ellipsoid, which is a graphical indicator of the similarity among all the samples and similar to the ANOVA results obtained earlier.

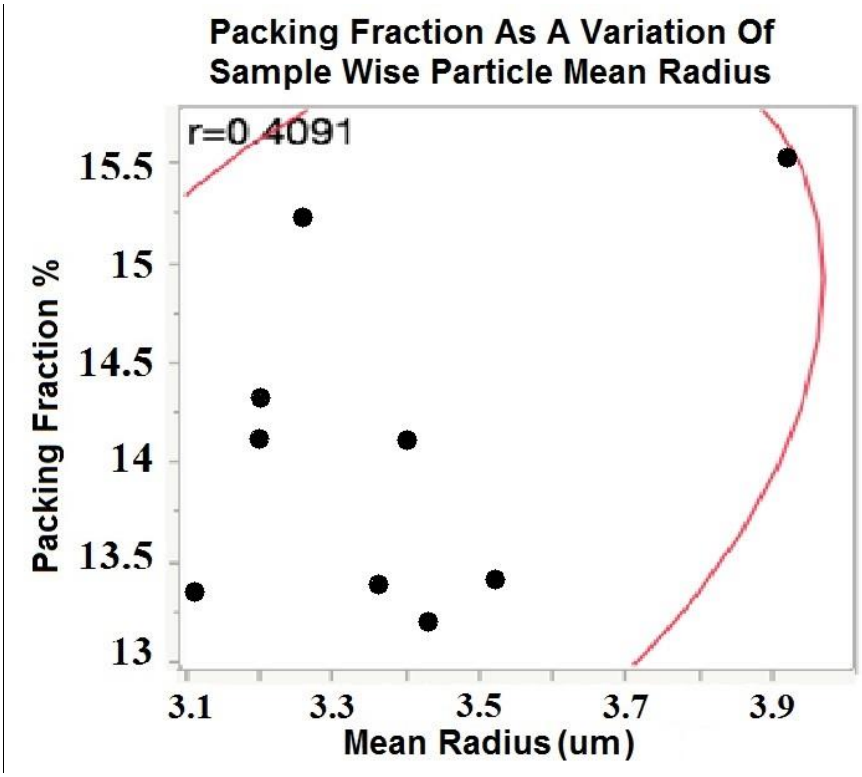

Figure 3.10: Sample wise Packing fraction – Mean Particle Radius (µm) correlation check. The Pearson's correlation coefficient 'r' was 0.4091 and correlation probability 'p' was 0.2742. We observe a weak correlation between the two parameters, indicating that the packing fraction is independent of the particle size in the samples.

This correlation was evaluated by the Pearson's correlation co-efficient 'r' and correlation probability p-value of the correlation. The Pearson's correlation co-efficient 'r' lies in the range of -1 to 1. An r-value of -1 or 1 denotes a stronger negative or positive correlation respectively, thereby

denoting a higher convergence of all the points in the study. An r-value of 0 denotes that there is no correlation among the data points. A p-value lesser than 0.05 indicates a strong correlation. This correlation with an r-value of 0.4091 and p-value of 0.2742 indicates a positive but weak correlation between packing fraction and sample mean radius.

CHAPTER 4: DISCUSSION & CONCLUSIONS

4.1: Discussion

Particles shown in the cross-sectional images contain darker regions within the lighter grey particle areas. These darker regions are indications of the presence of either hollows or a different material that is non-fluorescent residing inside the toner particles. Modern toners incorporate more than one binder resin [94]. The additional resin, typically a wax component, is to reduce the toner fixing/fusing temperature.

As indicated in chapter 2.3, the Z-position of the particle was estimated by comparisons of radius variation of the particle attained at different depths. It was possible to obtain the Z-position of the particle using the fluorescence intensity profile in the CLSM software, but the presence of the non-fluorescent wax component in the toner complicates the analysis with the fluorescence intensity profile. A larger diameter plane could correspond to less fluorescent intensity if much wax material exists within the particle and affects the summation of the fluorescence (pixels) in the sampling image plane. Because of this complication, for this study the researcher chose the radii comparison method for the Z-center analysis.

Analyses from both radii comparison and fluorescent intensity profile methods resulted in larger radius values in the Z direction as compared to those determined from the XY planes, addressing the Point Spread Function (PSF) phenomenon in optical microscopy [20-22]. The prolate spheroidal shape in Figure 3.1 was caused by the three-dimensional diffraction pattern of light emitted from a small ‘point’ source (toner in this case) in the sample.

To correct the artificial Z-radius elongation, the researcher made the assumption that the particles were spherical with radius values measured from the XY cross-sectional planes during the reconstruction, and that the PSF for a particle is the same for +Z and –Z directions.

The diffraction due to the use of glass slides can be used to explain the limitation of the sampling to a maximum of 5 layers of particles in a structure in this research. This is because the images taken beyond a certain Z position were dark and unclear due to interference from the fluorescence emissions of the lower layers of the particle structure. Earlier CLSM imaging methods for colloids dispersed the colloidal particles in a refractive index matching solvent to enable imaging of thicker layers of particles [62, 63, 66]. However, this research used particles in powder form and not dispersed in any colloidal solution, which increased the scattering of light, thereby reducing the resolution of the images and limited the sample scanning depth to around 35 μm. The correction of this phenomenon could be possible by switching the sample preparation accessories from glass to a thinner surface matching the refractive index of the polymer used in toner.

The methodology used in this thesis determined the packing fraction directly from the participating particles. The resulting measurement of 14.07 % ± 0.84 % compares well with the previously published packing fraction values of 14.7% from the studies using a simulation of highly cohesive particles [1, 31, 55], whereby it can be hypothesized that the

particle structure studied in this research roughly emulates Random Ballistic Deposition (RBD) simulated structures for cohesive particles. These results could also indicate that EP toners are cohesive particles. The correlation result of the packing fraction with the size of particles for the structures obtained in this research is in accordance with the literature findings for particle simulations [1, 31, 34, 42, 43]. An analysis of the particle layering in the samples showed that the base of the cluster contained the maximum number of particles, and the number of particles reduced gradually in each layer with increasing Z-axis [7, 11, 30, 39, 40, 44, 45]. The number of particles per layer in this study was found to be similar to the literature simulation calculations for the highest cohesiveness of the particles [45].

However, it is to be noted that in the calculation of the packing fraction, the volume cell considered may not represent the sample accurately. This could result in packing fractions lower than the actual packing density. Additionally, cartridge toner mixture contains micron-sized silica particles [94] smaller than toner which are non-fluorescent in nature and thus invisible during the imaging. If these silica particles are accounted for in the packing density calculations, the actual packing density could be relatively higher than our findings in this work, since the size of these particles is quite significant when compared to the size of the toner. This could be verified using X-ray μCT scanning as it has a better

resolution and is applicable to non-fluorescent particles unlike this study, which was discussed earlier.

Although different particle clusters were imaged and sample size (number of particles in the imaged cluster) was different for each sample, all our samples showed similar packing fraction values, thus potentially showing a similarity in the clustering of particles across all samples. An Analysis of Variance (ANOVA) comparison of the samples showed the similarity of the samples irrespective of the number of particles per sample, supported by an All-pairs Tukey-Kramer test result. The samples analyzed showed similar packing fraction values, which could indicate a similarity in the structural arrangement of the samples, implying that the clusters are self-similar. This is analogous to the findings reported in the previously published literature on self-similarity of agglomerated particle structures [55, 83, 84, 87]. Thus, a connotation can be drawn on the self-similar nature of the deposited particle clusters in this research. This proposition of self-similarity can be checked for in larger imaging areas (bigger XY planes) consisting of bigger particle clusters through improvements in the imaging and particle analysis methods to accommodate the scanning of denser particle structures.

4.2: Conclusions

This thesis has successfully developed a framework for the determination of particle coordinates and size in a packed particle structure using CLSM and Matlab. This mapping and reconstruction of particles in

3D space demonstrates the feasibility of reconstructing powder interiors and quantitatively characterize the packing fraction of the particle structures formed, using CLSM and Matlab. The packing fraction results validate the theoretical hypothesis of sticky particle deposition. An ANOVA and All-Pairs Tukey-Kramer test indicate the similarity of the samples, irrespective of the number of particles in each sample. Correlation analysis between particle size and packing fraction of the samples shows that the packing fraction parameter is weakly correlatable to the particle size. Similar packing fraction values were observed for all the samples analyzed, thus indicating a similarity in the structural arrangement of the particles in the clusters, implying that the clusters are self-similar. Thus, the CLSM has proven to be a feasible method of imaging structured fluorescent particles. Using Matlab, it is possible to analyze these images to deduce the particle coordinates and obtain their sizes for reconstruction of the 3-dimensional structure formed by these particles for further analysis of the structures.

CHAPTER 5: SUGGESTIONS FOR FUTURE RESEARCH

Suggestions for Future Research

This research has provided a head start for numerous paths of research down the line. While no external forces influenced the deposition of the powder during sample preparation in this research, new samples can be created in the presence of external forces like a voltage bias and analyzed using the framework developed in this work to obtain the packing fraction of the particle structures in non-sticky scenarios. More samples can be analyzed to check the relationship between the packing fraction and the particle radius to validate the results for the cohesive toner particles in this research. The samples mentioned in this research could be scanned using X-ray μCT technique for the verification of the particle packing fraction obtained in this literature, as non-fluorescent components of toner mixture were ignored in the CLSM imaging.

Improvements can be made in the sample preparation procedure to accommodate the scanning of multiple particle layers with better resolution for the analysis of bigger particle clusters without diffraction loss. The property of self-similarity of toner clusters can be confirmed by imaging and analyzing a big particle cluster consisting of hundreds to thousands of particles, breaking down the volume cell randomly into smaller volume cells, analyzing the smaller volume cells and comparing the packing fractions of these smaller volume cells to that of the bigger volume cell. If the packing fraction results are comparable, this will elucidate the self-similarity of the particle structures used in this research. Further analysis

will help reveal the fractal dimension D value which has been calculated for particle structures through simulations and experiments in literature [82, 83, 86, 90].

It is possible to extend the particle analysis algorithm to obtain particle parameters like particle coordination number, contact angle and area of contact of the particle with the surrounding particles. An investigation using the Discrete Element Method (DEM) simulation could be performed to obtain the inter particle parameters like contact angle, coordination number, contact forces and trajectories of particles for the reconstructed samples, as DEM focuses on particle simulations of higher complexity [42, 43]. This will be useful in the calculation of the forces acting on the particle in the sample, while providing an overview of the mechanical properties of the sample. These calculations will provide an insight on the interaction of a single particle with neighboring particles and help understand the structure from the particle perspective.

The particle detection algorithm can be extended for the faster analysis of samples with higher number of particles. The automation of this particle analysis procedure will reduce the processing time per sample from hours to minutes, enabling a faster analysis of the particle structures for comparison with simulations and further assist the analysis of structures with large number of particles. This algorithm is not necessarily limited to the CLSM imaging technology used in this work, but also applicable to other imaging technologies which generate images through the digital

slicing of the objects. Thus, the particle detection algorithm can be modified to align with other non-destructive imaging technologies like X-ray μCT [72-74, 77, 82, 95] and Automated Serial Sectioning Tomography [81], where, particles in granular material structures can be quantified from the analysis of the digitally sliced sample images using the particle detection algorithm.

REFERENCES

[1] H. Mizes, "The Structure of Toner Sediments Simulated with Random Ballistic Deposition," in *International Conference on Digital Printing Technologies*, pp. 495-498, 1999.

[2] I. Gibson, D. W. Rosen, and B. Stucker, *Additive manufacturing technologies*: Springer, 2010.

[3] L. E. Murr, *et al.*, "Fabrication of Metal and Alloy Components by Additive Manufacturing: Examples of 3D Materials Science," *J. Mater. Res. Tech.*, vol. 1, pp. 42-54, 2012.

[4] N. Sudarmadji, J. Y. Tan, K. F. Leong, C. K. Chua, and Y. T. Loh, "Investigation of the mechanical properties and porosity relationships in selective laser-sintered polyhedral for functionally graded scaffolds," *Acta Biomaterialia*, vol. 7, pp. 530-537, 2011.

[5] D. A. Ramirez, *et al.*, "Novel precipitate–microstructural architecture developed in the fabrication of solid copper components by additive manufacturing using electron beam melting," *Acta Materialia*, vol. 59, pp. 4088-4099, 2011.

[6] J. A. Choren, S. M. Heinrich, and M. B. Silver-Thorn, "Young's modulus and volume porosity relationships for additive manufacturing applications," *J. Mater. Sci.*, vol. 48, pp. 5103-5112, 2013.

[7] R. Jullien and P. Meakin, "Simple Three-Dimensional Models for Ballistic Deposition with Restructuring," *Europhys. Lett.*, vol. 4, p. 1385, 1987.

[8] R. Jullien, and P. Meakin, "Random sequential adsorption with restructuring in two dimensions," *J. Phys. A: Math. Gen.*, vol. 25, p. L189, 1992.

[9] A. Pavlovitch, R. Jullien, and P. Meakin, "Geometrical properties of a random packing of hard spheres," *Phys. A: Stat. Mech. Appl.,* vol. 176, p. 206-219, 8/15/1991.

[10] P. Meakin, "Computer Simulation of Growth and Aggregation Processes," *On Growth and Form*. vol. 100, p. 111-135, 1986.

[11] P. Meakin and R. Jullien, "Ballistic deposition with sticky and non-sticky particles," *Phys. A: Stat. Mech. Appl.,* vol. 175, p. 211-221, 7/1/1991.

[12] S. Kim, J. Henderson, and P. Chaudhari, "Computer simulation of amorphous thin films of hard spheres," *Thin Solid Films,* vol. 47, p. 155-158, 12/1/1977.

[13] P. Schaaf and J. Talbot, "Kinetics of Random Sequential Adsorption," *Phys. Rev. Lett.,* vol. 62, p. 175-178, 01/09/1989.

[14] J. Talbot, and S. M. Ricci, "Analytic model for a ballistic deposition process," *Phys. Rev. Lett.,* vol. 68, p. 958-961, 02/17/1992.

[15] J. Zhou, Y. Zhang, and J. K. Chen, "Numerical Simulation of Random Packing of Spherical Particles for Powder-Based Additive Manufacturing," *J. Manuf. Sci. Eng.,* vol. 131, p. 031004, 2009.

[16] P. A. Cundall and O. D. L. Strack, "Modeling of microscopic mechanisms in granular material," *Mech. Gran. Mat.s: New Models and Constitutive Relations,* vol. 63, 2013.

[17] A. V. Kumar and A. Dutta, "Electrophotographic Layered Manufacturing," *J. Manufac. Sci. Eng.,* vol. 126, pp. 571-576, 2004.

[18] J. B. Jones, Wimpenny, D. I., Chudasama, R. and Gibbons, G. J., "Printed Circuit Boards by Selective Deposition and Processing,", 22nd Solid Freeform Fabrication Symposium Austin, TX, USA, 2011, pp. 639-656.

[19] J. Jones, D. Büttner, R. Chudasama, D. Wimpenny, and K. Krüger, "Laser Printing Circuit Boards and Electronics," *J. Ima. Sci. Tech.,* vol. 56, pp. 40503-1 - 40503-11, 2012.

[20] M. Bartzsch, H. Kempa, M. Otto, A. Hübler, and D. Zielke, "Device and circuit simulation of printed polymer electronics," *Org. Elec.*, vol. 8, pp. 431-438, 2007.

[21] F. K. W. Lee and H.-T. Chuah, "A Finite-Difference Time-Domain (FDTD) Software for Simulation of Printed Circuit Board (PCB) Assembly," *Prog. Electromag. Res.,* vol. 50, pp. 299-335, 2005.

[22] S. Ray, B. Mal, and J. Shamanna, "Generalized ballistic deposition in 2 dimensions: scaling of surface width, porosity and conductivity," *arXiv preprint arXiv:1503.01047,* 2015.

[23] G. G. Guilbault, *Practical Fluorescence*, Second ed.: CRC Press, October 26, 1990.

[24] J. B. Pawley and B. R. Masters, *Handbook of Biological Confocal Microscopy, Third Edition* vol. 13: International Society for Optics and Photonics, 2008.

[25] S. R. P. Pavani, *et al.,* "Three-dimensional, single-molecule fluorescence imaging beyond the diffraction limit by using a double-helix point spread function," *Proceedings of the National Academy of Sciences*, vol. 106, pp. 2995-2999, 2009.

[26] D. Lafreniere, C. Marois, R. Doyon, D. Nadeau, and t. Artigau, "A New Algorithm for Point-Spread Function Subtraction in High-Contrast Imaging: A Demonstration with Angular Differential Imaging," *Astrophys. J.*, vol 660, p. 770, 2007.

[27] B. Zhang, J. Zerubia, and J.C. Olivo-Marin, "Gaussian approximations of fluorescence microscope point-spread function models," *Appl. Opt.,* vol. 46, p. 1819-1829, 2007.

[28] R. O. Duda, and P. E. Hart, "Use of the Hough transformation to detect lines and curves in pictures," *Comm. ACM,* vol. 15, p. 11-15, 1972.

[29] G. Siogkas, *Visual Media Processing Using Matlab Beginner's Guide*: Packt Publishing Ltd, September 24, 2013.

[30] S. Chang, *et al.*, "Measurement of Toner Cohesion in Liquid Inks Using a Visualization Cell," *NIP & Digital Fabrication Conference,* vol. 1998, pp. 218-221, 1998.

[31] T. Kitamura, N. Mizuno, S. Nakamura, and K. Hoshino, "Improvement of Image Contrast in Toner Display," *NIP & Digital Fabrication Conference,* vol. 2004, pp. 1005-1007, 2004.

[32] K. K. C. Kumara, S. Suzumi, S. Nakamura, N. Miyagawa, and T. Kitamura, "Effects of Triboelectrical Charge of Toners on Display Characteristics of Toner Display," *NIP & Digital Fabrication Conference,* vol. 2010, pp. 520-522, 2010.

[33] T. Kitamura, M. Takeuchi, S. Nakamura, and N. Miyagawa, "Control of Particle Movement for Color Toner Display," *NIP & Digital Fabrication Conference,* vol. 2007, pp. 633-635, 2007.

[34] J. Blum and R. Schräpler, "Structure and Mechanical Properties of High-Porosity Macroscopic Agglomerates Formed by Random Ballistic Deposition," *Phys. Rev. Lett.*, vol. 93, p. 115503, 09/10/2004.

[35] R. Jullien and P. Meakin, "Concentration effects in random ballistic deposition with restructuring," *J. Phys. A: Math. Gen.*, vol. 22, p. L219, 1989.

[36] P. K. Watson, H. Mizes, A. Castellanos, and A. Perez, "The packing of fine, cohesive powders," *Powders & Grains 97*, pp. 109-112, 1997.

[37] F. A. Gilabert, J. N. Roux, and A. Castellanos, "Computer simulation of model cohesive powders: Plastic consolidation, structural changes, and elasticity under isotropic loads," *Phys. Rev. E,* vol. 78, p. 031305, 09/15/2008.

[38] E. A. Gulliver, "Simulation of mixture microstructures via particle packing models and their direct comparison with real mixtures," Rutgers The State University of New Jersey, 2003.

[39] T. Jia, Y. Zhang, and J. K. Chen, "Dynamic Simulation of Particle Packing With Different Size Distributions," *J. Manuf. Sci. Eng.,* vol. 133, p. 021011, 2011.

[40] A. Tewari and A. M. Gokhale, "Nearest-neighbor distances between particles of finite size in three-dimensional uniform random microstructures," *Mat. Sci. Eng.: A,* vol. 385, p. 332-341, 11/15/2004.

[41] A. Tewari, and A. M. Gokhale, "Nearest neighbor distances in uniform–random poly-dispersed microstructures," *Mat. Sci. Eng.: A,* vol. 396, p. 22–27, 2005.

[42] J. J. Ramsden, "Review of new experimental techniques for investigating random sequential adsorption," *J. Stat. Phys.,* vol. 73, p. 853-877, 1993.

[43] P. R. Johnson and M. Elimelech, "Dynamics of Colloid Deposition in Porous Media: Blocking Based on Random Sequential Adsorption," *Langmuir,* vol. 11, pp. 801-812, 1995.

[44] P. Meakin and J. Krug, "Columnar Microstructure in Three-Dimensional Ballistic Deposition," *Europhys. Lett.,* vol. 11, p. 7, 1990.

[45] M. J. Vold, "The Sediment Volume in Dilute Dispersions of Spherical Particles," *J. Phys. Chem.,* vol. 64, p. 1616-1619, 1960.

[46] M. J. Vold, "Sediment Volume and Structure in Dispersions of Anisometric Particles," *J. Phys. Chem.,* vol. 63, pp. 1608-1612, 1959.

[47] T. Jia, Y. Zhang, J. K. Chen, and Y. L. He, "Dynamic simulation of granular packing of fine cohesive particles with different size distributions," *Powd. Tech.,* vol. 218, pp. 76-85, 2012.

[48] T. Jia, Y. Zhang, and J. K. Chen, "Simulation of granular packing of particles with different size distributions," *Comp. Mater. Sci.,* vol. 51, pp. 172-180, 2012.

[49] R. Jullien, and P. Meakin, "Ballistic Deposition and Segregation of Polydisperse Spheres," *Europhys. Lett.,* vol. 6, p. 629, 1988.

[50] P. Meakin and J. Krug, "Three-dimensional ballistic deposition at oblique incidence," *Phys. Rev. A,* vol. 46, pp. 3390-3399, 09/01/1992.

[51] A. Castellanos, J. M. Valverde, A. T. Pérez, A. Ramos, and P. K. Watson, "Flow Regimes in Fine Cohesive Powders," *Phys. Rev. Lett.,* vol. 82, pp. 1156-1159, 02/08/1999.

[52] B. Mal, S. Ray, and J. Shamanna, "Surface properties and scaling behavior of a generalized deposition model," ed. arXiv preprint arXiv:1410.6600, 2014.

[53] K. Banerjee, J. Shamanna, and S. Ray, "Surface morphology of a modified ballistic deposition model," *Phys. Rev. E,* vol. 90, p. 022111, 08/11/2014.

[54] M. Saadatfar, "Computer Simulation of Granular Materials," *Comp. Sci. Eng.,* vol. 11, pp. 66-74, 2009.

[55] J. M. Valverde and A. Castellanos, "Random loose packing of cohesive granular materials," *Europhys. Lett.,* vol. 75, p. 985, 2006.

[56] A. S. Clarke and H. Jónsson, "Structural changes accompanying densification of random hard-sphere packings," *Phys. Rev. E,* vol. 47, pp. 3975-3984, 06/01/1993.

[57] P. N. Pusey, W. van Megen, P. Bartlett, B. J. Ackerson, J. G. Rarity, and S. M. Underwood, "Structure of crystals of hard colloidal spheres," *Phys. Rev. Lett.,* vol. 63, pp. 2753-2756, 12/18/1989.

[58] A. C. Hoffmann and H. J. Finkers, "A relation for the void fraction of randomly packed particle beds," *Pow. Tech.,* vol. 82, pp. 197-203, 1995.

[59] W. C. K. Poon, E. R. Weeks, and C. P. Royall, "On measuring colloidal volume fractions," *Soft Matter,* vol. 8, pp. 21-30, 2012.

[60] K. N. Amato, *et al.,* "Microstructures and mechanical behavior of Inconel 718 fabricated by selective laser melting," *Acta Materialia,* vol. 60, pp. 2229-2239, 2012.

[61] L. E. Murr, *et al.,* "Fabrication of Metal and Alloy Components by Additive Manufacturing: Examples of 3D Materials Science," *J. Mat. Res. and Tech.,* vol. 1, pp. 42-54, 2012.

[62] A. D. Dinsmore, E. R. Weeks, V. Prasad, A. C. Levitt, and D. A. Weitz, "Three-Dimensional Confocal Microscopy of Colloids," *Appl. Opt., Vol. 40, Issue 24,* p. 4152-4159, 2001.

[63] V. Prasad, D. Semwogerere, and E. R. Weeks, "Confocal microscopy of colloids," *J. Phys.: Cond. Matt.,* vol. 19, p. 113102, 2007.

[64] P. Schall, I. Cohen, D. A. Weitz, and F. Spaepen, "Visualization of Dislocation Dynamics in Colloidal Crystals," *Science,* vol. 305.5692, pp. 1944-1948, 2004.

[65] M. C. Jenkins and S. U. Egelhaaf, "Confocal microscopy of colloidal particles: Towards reliable, optimum coordinates," *Adv. Col. Interf. Sci.,* vol. 136, pp. 65-92, 1/15/2008.

[66] T. H. Besseling, M. Hermes, A. Kuijk, B. de Nijs, T.-S. Deng, M. Dijkstra, A. Imhof, and A. van Blaaderen, "Determination of the positions and orientations of concentrated rod-like colloids from 3D microscopy data," *J. Phys.: Cond. Matt.*, vol. 27, p. 194109, 2015.

[67] P. J. Schilling, B. R. Karedla, A. K. Tatiparthi, M. A. Verges, and P. D. Herrington, "X-ray computed microtomography of internal damage in fiber reinforced polymer matrix composites," *Compo. Sci. Tech.*, vol. 65, pp. 2071-2078, 2005.

[68] S. Van Bael, G. Kerckhofs, M. Moesen, G. Pyka, J. Schrooten, and J. P. Kruth, "Micro-CT-based improvement of geometrical and mechanical controllability of selective laser melted Ti6Al4V porous structures," *Mater. Sci. Eng.: A*, vol. 528, pp. 7423-7431, 9/15/2011.

[69] J. S. U. Schell, M. Renggli, G. H. van Lenthe, R. Müller, and P. Ermanni, "Micro-computed tomography determination of glass fibre reinforced polymer meso-structure," *Compo. Sci. Tech.*, vol. 66, pp. 2016-2022, 2006.

[70] H. Shen, S. Nutt, and D. Hull, "Direct observation and measurement of fiber architecture in short fiber-polymer composite foam through micro-CT imaging," *Compo. Sci. Tech.*, vol. 64, pp. 2113-2120, 2004.

[71] E. Andò, S. Hall, G. Viggiani, J. Desrues, and P. Bésuelle, "Grain-scale experimental investigation of localised deformation in sand: a discrete particle tracking approach," *Acta Geotechnica*, vol. 7, pp. 1-13, 2012.

[72] J. Desrues, *et al.*, "Void ratio evolution inside shear bands in triaxial sand specimens studied by computed tomography," *Géotechnique*, vol. 46, pp. 529-546, 1996.

[73] K. Lu, E. Sourty, R. Guerra, G. Bar, and J. Loos, "Critical Comparison of Volume Data Obtained by Different Electron Tomography Techniques," *Macromolecules,* vol. 43, pp. 1444-1448, 2010/02/09 2010.

[74] R. I. Al-Raoush and C. S. Willson, "Extraction of physically realistic pore network properties from three-dimensional synchrotron X-ray microtomography images of unconsolidated porous media systems," *Journal of Hydrology,* vol. 300, pp. 44-64, 1/10/2005.

[75] R. I. Al-Raoush, K. Thompson, and C. S. Willson, "Comparison of Network Generation Techniques for Unconsolidated Porous Media," *Soil Science Society of America Journal,* vol. 67, pp. 1687-1700, 2003.

[76] G. Viggiani, *et al.*, "X-ray microtomography for studying localized deformation in fine-grained geomaterials under triaxial compression," *Comptes Rendus Mécanique,* vol. 332, pp. 819-826, 2004.

[77] M. Myllys, H. Häkkänen, J. Korppi-Tommola, K. Backfolk, P. Sirviö, and J. Timonen, "X-ray microtomography and laser ablation in the analysis of ink distribution in coated paper," *J. Appl. Phys.,* vol. 117, p. 144902, 2015.

[78] G. R. Davis, A. N. Z. Evershed, and D. Mills, "Characterisation of materials: determining density using X-ray microtomography," *Mater. Sci. Tech.,* vol. 31, pp. 162-166, 2015.

[79] C. Gupta, E. van de Casteele, M. Wevers, H. Hoshino, M. Kobayashi, and A. Biswas, "Quantitative 3D characterisation of porous NiTi fabricated by self-propagating high temperature synthesis using X-ray microtomography," *Mater. Sci. Tech.,* vol. 31, pp. 594-602, 2014.

[80] J. Martín-Herrero and C. Germain, "Microstructure reconstruction of fibrous C/C composites from X-ray microtomography," *Carbon,* vol. 45, pp. 1242-1253, 2007.

[81] E. Pirard, "3D Imaging of Individual Particles: A Review," *Image Anal. Stereol.,* vol. 31, p. 13, 2012-06-14 2012.

[82] C. Kranenburg, "The Fractal Structure of Cohesive Sediment Aggregates," *Estuarine, Coastal and Shelf Science,* vol. 39, pp. 451-460, 1994.

[83] D. W. Schaefer, J. E. Martin, P. Wiltzius, and D. S. Cannell, "Fractal Geometry of Colloidal Aggregates," *Phys. Rev. Lett.,* vol. 52, pp. 2371-2374, 06/25/1984.

[84] R. Desai, A. Denton, H. Stanley, and N. Ostrowski, "On Growth and Form," *Nijhoff, Dordrecht,* p. 237, 1986.

[85] F. A. Gilabert, J. N. Roux, and A. Castellanos, "Computer simulation of model cohesive powders: Influence of assembling procedure and contact laws on low consolidation states," *Phys. Rev. E,* vol. 75, p. 011303, 01/10/2007.

[86] E. Goudeli, M. L. Eggersdorfer, and S. E. Pratsinis, "Coagulation–Agglomeration of Fractal-like Particles: Structure and Self-Preserving Size Distribution," *Langmuir,* vol. 31, pp. 1320-1327, 2015.

[87] P. Tandon and D. E. Rosner, "Monte Carlo Simulation of Particle Aggregation and Simultaneous Restructuring," *J. Col. Interf. Sci.,* vol. 213, pp. 273-286, 5/15/1999.

[88] D. A. Weitz and M. Oliveria, "Fractal Structures Formed by Kinetic Aggregation of Aqueous Gold Colloids," *Phys. Rev. Lett.,* vol. 52, pp. 1433-1436, 04/16/1984.

[89] J. S. Leszczynski, "A discrete model of a two-particle contact applied to cohesive granular materials," *Gran. Matt.,* vol. 5, pp. 91-98, 2003.

[90] P. Meakin, "Fractal aggregates," *Adv. Coll. Interf. Sci.,* vol. 28, pp. 249-331, 1988.

[91] S. Chang, V. R. Patil, D. Bai, and M. Esterman, "Direct Three-Dimensional Visualization and Characterization of Microstructures Formed by Printing Particles," *NIP & Digital Fabrication Conference*, vol. 2014, pp. 320-325, 2014.

[92] D. Bai, V. R. Patil, M. Esterman, and S. Chang, "Characterizing Three Dimensional Microstructures Formed By Particles: An Example of Electrophotographic Printing Toner," 2014 Solid Freeform Fabrication Symposium, 2014.

[93] S. Chang, V. Patil, D. Bai, and M. Esterman, "Direct visualization and three-dimensional reconstruction of structures formed by electrophotographic toner," *Powd. Tech.*, vol. 269, pp. 1-6, 2015.

[94] S. Matsunaga, M. Ohno, T. Onuma, M. Shimojo, and C. K. Kaisha, "Toner with wax component for developing electrostatic image", Pat. US 5605778 A, 1997.

[95] B. Zhao, J. Wang, M. R. Coop, G. Viggiani, and M. Jiang. "An investigation of single sand particle fracture using X-ray micro-tomography", *Géotechnique 65*, 625-641, 2015.

APPENDIX

1. **Microscope Sample Preparation:**
    a. Wear protective clothing and gear – coat, safety glasses and safety gloves before handling toner.
    b. Obtain a microscopy glass slide, use thick double-sided tape to create an enclosed square dam on the slide. Allow to dry.
    c. Obtain toner from the source and drop small quantities on a microscopy cover slip.
    d. Stick the glass slide on the cover slip to enclose the toner within the square dam without disturbing the structure formed by the toner.
    e. Allow the specimen to dry. This dried specimen is ready to use for CLSM imaging.

2. **CLSM Settings:**
    a. Mode: Fluorescence
    b. Scan Mode: XYZ
    c. Excitation λ (nm): 465nm
    d. Emission collection range λ (nm): 475nm to 610nm
    e. Objective: 40X
    f. Additional refractive medium (on Objective): Water
    g. Step size: 170nm or 0.17μm

3. **Particle Detection Algorithm:**
    a. Start.
    b. Image the sample in XYZ mode using the CLSM.
    c. Generate the images from the imaging in .jpeg format and convert to grayscale.
    d. Analyze each particle's Z centroid through particle radius analysis in all images.
    e. Generate the Z position vs XY particle radius for each particle to obtain the Z centroid.

f. Process the Z centroid image using the Particle Detection Matlab code to obtain the X & Y positions and XY particle radius in the image dimensions.
g. Generate the XYZ coordinates and assume the particle to be spherical with radius = XY radius.
h. Obtain a 3-dimensional reconstruction of the sample using Matlab.
i. Stop.

4. Particle Detection Matlab Code:

```
% This is a Matlab script for the automation of the process of finding the XYZ

% coordinates and the radius of particles from the confocal image files.

% Steps include - 1. Extract the maximum height values from the .csv

% file of the series for the particular ROIs. 2. Calculate the frame number

% for that ROI. 3. Run imfindcircles on that frame and extract the

% exact coordinate of that particle

% Author - Vineeth Patil

% Last updated - 5/13/2015

% ©RIT SMS


% Input the name of the csv file in the folder. CSV file needs to be generated

% from the Confocal .lif file

url = '*enter complete path to the source csv file here within the quotes*';

row = 0;

col = 0;
```

```
Max_pos = csvread(url,row,col,'Insert columns here')  % To insert columns, 'V11..AM11' is the format to be followed for reading the rows and columns from the csv using csvread

itemp = 1; % set a temporary counter


% defining the step size

step_size = 0.17;


% defining the minimum and maximum radius values

RMin = 20;

RMax = 100;


% Set current directory to the respective folder with the images to analyze

cd Series022Full;  % Enter the directory name in place of Series022Full where
                   % all the images of the CLSM sample stack are present


while itemp <= 100 %Set the max itemp


    frame_number = round(Max_pos(itemp)/step_size)

    itemp = itemp + 1; %set itemp increase counter
```

```
% Usually CLSM image files are prefixed with an index consisting of Sample series name, followed by file type
   if (frame_number<100)
      filePrefix = 'Series022_z0';
   else if (frame_number>=100)
         filePrefix = 'Series022_z';
      end
   end
   fileName = num2str(frame_number);
   fileExtension = '.jpg';    % This can be changed to .bmp or .tif based on
                              % the file format of the images being analyzed
   fileString = [filePrefix fileName fileExtension]

   %Read the image with the filename and show it as an rgb image
   rgb = imread(fileString);

   %Convert the image to grayscale
   gray = rgb2gray(rgb);

   % The imfindcircles finds the centers and radii of the spheres which are of
   % the size 12 to 16 pixels with a bright object polarity, as the particles
   % appear as green. The sensitivity of the program is set at 0.75
```

```
    [centers, radii] = imfindcircles(gray,[RMin RMax], 'ObjectPolarity','bright', 'Sensitivity',0.95, 'EdgeThreshold',0.10)


    % Input the dimensions of the scan and the pixel resolution of the image.
     % 44.52 microns is the size of the image used in my analysis
     % This dimension can vary based on your sample size. The image resolution is set
     % to a default of 1024. This can be changed based on the image resolution
    dimension = 44.52;
    pixels = 1024;


    % This converts the X & Y coordinates of the particles from pixels to
    % microns
     XY_coordinates_in_microns = (dimension*centers)/pixels


    % This converts the radii of the particles from pixels to microns
     Radii_in_microns = (dimension*radii)/pixels
end % End of the program
```